Effect of manganese promotion on the activity and selectivity of cobalt catalysts for CO preferential oxidation

Effect of Manganese Promotion on the Activity and Selectivity of Cobalt for CO Preferential Oxidation

Liping Zhong,[a], Mathias Barreau,[a,*] Dingkai Chen,[a] Valerie Caps,[a] Michael Haevecker,[b,c] Detre Teschner, [b,c] David H. Simonne,[d] Elisa Borfecchia,[d] Walid Baaziz,[e] Břetislav Šmíd,[f] and Spyridon Zafeiratos,[a,*]

[a]*Institut de Chimie et Procédés pour l'Energie, l'Environnement et la Santé (ICPEES), ECPM, UMR 7515 CNRS – Université de Strasbourg, 25 rue Becquerel, 67087 Strasbourg Cedex 02, France*

[b]*Max-Planck-Institut für Chemische Energiekonversion (MPI-CEC), Stiftstrasse 34-36, D-45470 Mülheim a.d. Ruhr, Germany*

[c]*Fritz-Haber-Institut der Max-Planck-Gesellschaft, Faradayweg 4-6, D-14195 Berlin, Germany*

[d]*Department of Chemistry, INSTM Reference Center and NIS Centers, University of Torino, Via P. Giuria 7, 10125 Torino, Italy*

[e]*Institut de Physique et Chimie des Matériaux de Strasbourg (IPCMS), UMR 7504 CNRS – Université de Strasbourg, 23 rue du Loess BP 43, 67034 Strasbourg cedex 2, France*

[f]*Charles University, Faculty of Mathematics and Physics, Department of Surface and Plasma Science, V Holešovičkách 2, 18000, Prague 8, Czech Republic*

Abstract

The preferential oxidation of CO in H_2-rich mixtures (COPrOx) is a major catalytic reaction utilized for hydrogen purification. In the exploration of alternatives to noble metals, the cobalt-based catalysts appear to be a very promising choice. The activity and stability of cobalt in the COPrOx reaction can be improved by addition of transition metals and manganese is the most prominent among them. Yet, few studies have been focused to understand the reason that makes manganese promotion so beneficial for cobalt catalytic performance. Here, we compare pure and Mn-modified cobalt catalysts for COPrOx and correlate the catalytic performance with the characterization of their surface monitored by *operando* spectroscopic methods (NAP-XPS and NEXAFS). The Mn-promoted cobalt catalyst is significantly more active, and has higher CO_2 selectivity than pure cobalt especially at intermediate reaction temperatures (around 200 °C). The addition of Mn improves the thermal stability of the catalyst and helps to maintain higher specific surface areas. Detailed surface analysis suggests that Mn is not directly involved in the reaction, but its main function is to stabilize the CoO phase on the surface, hence promoting CO conversion. It is also suggested that at high COPrOx reaction temperatures Mn suppresses methanation.

Keywords : COPrOx; cobalt oxides; manganese oxides; mixed oxides; selectivity; operando spectroscopy; NAP-XPS; NEXAFS

1 Introduction

CO preferential oxidation (COPrOx) is one of the most straightforward and efficient methods to eliminate CO from hydrogen-feed for utilization as fuel in proton-exchange membrane fuel cells (PEMFCs) [1–4]. An ideal COPrOx catalyst should be highly selective to CO oxidation but not to H_2 oxidation and CO methanation reactions [4]. Platinum group metals (Ru, Au, Pt) supported on various oxides can achieve 100% of CO conversion in the hydrogen feed at relatively low temperature [5–7]. However, the high price and limited availability of noble materials have urged the development of COPrOx catalysts based on non-noble transition metals (Cu, Co, Ni) [8–11]. Among them, Cu oxides supported on CeO_2 have comparable performance to noble metal catalysts [12–14]. The excellent activity of CuO-CeO_2 system was attributed to the remarkable oxygen-storage/releasing capacity of ceria and the change transfer between Cu^{2+}/Cu^{+} and Ce^{4+}/Ce^{3+} [15,16].

Besides copper, cobalt oxide catalysts are known to be active for CO oxidation especially at very low temperatures (down to -77 °C) [17]. Moreover, Co_3O_4 nanostructures with certain morphologies [18] or deposited on befitting supports, have displayed excellent activity for COPrOx [19–24]. Nevertheless, so far, the reported cobalt-based catalysts cannot yet meet the requirements for successful commercialization in COPrOx reaction. The high onset temperature of CO oxidation under COPrOx conditions, CO methanation at higher temperature and the fast deactivation of the catalyst are the main performance deficiencies [25]. The performance of cobalt oxide catalysts can be improved by promotion with an additional oxide [26,27]. Among them, MnO_x and CeO_2 additives/promoters have shown the most promising COPrOx catalytic performance [27–39].

Notably several groups have reported that Mn surpass any other metal promoter and boosts cobalt catalysts performance for both CO oxidation [27,28,38,39,29–32,34–37] and COPrOx reactions [36,40,41]. The positive effect of manganese is not well understood, but some authors speculated that MnO_x contribute to the stabilization of Co^{3+} species at the surface by facilitating oxidation of Co^{2+} to Co^{3+} [27,31]. This hypothesis assumes that Co^{3+} sites of Co_3O_4 are the active sites for COPrOx which opposes our recent findings about the detrimental role of Co_3O_4 in the activity [42]. This evident contradiction was the driving force to investigate in detail the promotional effect of Mn on Co for COPrOx in this work. Manganese oxides are active for CO oxidation [43], but there are no reports regarding their intrinsic activity as compared to cobalt oxides, neither about their selectivity in H_2-rich mixtures. Similar to cobalt, the reactivity of manganese oxides is affected by their oxidation state in the order: $MnO<MnO_2<Mn_2O_3$ at 250 °C [44,45]. This indicates that the oxidation state of manganese may also play an essential role for CO conversion on Mn-Co catalyst. However, to the best of the authors' knowledge the evolution

of Mn oxidation state in Co-Mn system during the COPrOx has never been studied in detail. This provides an additional motivation for the study of Co-Mn using *in situ* surface sensitive methods. In a more general context, understanding the interaction of the elements in a hybrid catalyst is of importance for catalyst's development.

Accordingly, this study is devoted to describe the interaction between cobalt and manganese under COPrOx conditions and the relation between their surface oxidation states and the resulting catalytic performance. Based on literature, the Co:Mn = 1:0.125 mixing ratio seems to be optimal for COPrOx [36,41]. Therefore, in this work we did not try to optimize the Co-Mn catalyst composition, but we used the one reported (Co_8MnO_x) to have the best activity [36,41]. Two other unsupported catalysts (CoO_x and $CoMn_8O_x$) were also prepared and used for comparison. In addition to the conventional *ex situ* structural and morphological characterization (H_2-TPR, XRD, SEM, BET), X-ray spectroscopic techniques (NAP-XPS and NEXAFS), including both synchrotron and laboratory based-experiments, were used to investigate *in situ* the evolution of each component during COPrOx.

2 Materials and Methods

2.1 Catalysts preparation

Commercially available nanoparticulate cobalt monoxide (CoO, 99.99%, Sigma Aldrich CAS# 1307-96-6) was used as catalyst in its pure form (CoO_x), or as a support for the synthesis of the Co-Mn catalyst (Co_8MnO_x). The Co_8MnO_x catalyst was synthesized by incipient wetness impregnation method. In details, 0.5025g of Manganese (II) nitrate tetrahydrate ($Mn(NO_3)_2.4H_2O$) was dissolved in 0.317g of water. The obtained solution was added to 1.2 g CoO and the obtained mixture was dried in air at 120 °C for 12 h. The dry product was subsequently calcined in air at 400°C for 3h. The same synthesis method was used for the preparation of the reference $CoMn_8O_x$ catalyst (the atomic ratio of Co/Mn was 1/8 in this case), however, in this case Mn_3O_4 acted as support and was impregnated with the cobalt-containing solution. In details, 1.83 g of commercial Mn_3O_4 was impregnated with an aqueous solution of 0.582g of $Co(NO_3)_2.6H_2O$ in 0.144 g of water. Then, the mixture was dried for 12 h at 120 °C and subsequently calcined in air for 3 h at 400 °C.

2.2 Catalytic tests

The catalytic oxidation of CO in the presence of H_2 was performed in a fully automated fixed-bed flow reactor (CETRIB SARL, Andlau, France) [46,47]. 50 mg of the catalytic powder was introduced in a quartz glass tube (i.d. 10 mm) and dispersed evenly on a P3 glass frit (16-40 μm). Average thickness of the catalytic bed was about 1 mm. The glass reactor was then introduced in a tubular oven with the catalyst bed located in the isothermal zone. Gas mixtures were generated

using calibrated (Serv's Instrumentation) mass flow controllers (Bronkhorst). The COPrOx gas mixture was composed of 1% CO, 1% O_2, 50% H_2 balanced in helium. The feed gas was introduced in reactor at a total flow rate of 50 mL·min^{-1} (1 atm, GHSV ~ 7,500 h^{-1}). The temperature was monitored by a type K thermocouple plunged inside the catalytic bed. The reactants and products were monitored by a Compact Gas Chromatograph (CGC from Interscience, Belgium) equipped with a TCD detector. Prior to each test, the pre-reduced catalyst was reduced once again *in situ,* by using the following protocol: heating at 400°C for 30 min in 100% H_2 (50 mL·min^{-1}) with a heating rate of 10°C·min^{-1} and cooling back down to 30°C. The residual oxygen content of the gas phase was below 100 ppm. For light-off tests, the catalyst was heated under the COPrOx mixture to 50, 100, 150, 200, 250, 300 and 350°C using a ramp of 10°C·min^{-1} and dwell time of 30 min at each temperature. The CO and O_2 (X_{CO}, X_{O2}) conversion as well as the selectivities ($S_{CO2}$and S_{CH4}) were calculated as follows:

$$X_{CO,T}\ (\%) = \frac{A_{CO,30°C} - A_{CO,T}}{A_{CO,30°C}} \times 100$$

$$X_{O2,T}\ (\%) = \frac{A_{O2,30°C} - A_{O2,T}}{A_{O2,30°C}} \times 100$$

$$S_{CO2,T}\ (\%) = \frac{1}{2} \times \frac{A_{CO,30°C} - A_{CO,T}}{A_{O2,30°C} - A_{O2,T}} \times 100$$

$$S_{CH4,T}\ (\%) = \frac{A_{CH4,T}\mathrm{RF_{CH4}}}{A_{CO,30°C} - A_{CO,T}} \times 100$$

where: $A_{i,30°C}$ and $A_{i,T}$ are the areas of the corresponding GC peaks at 30°C (no reaction) and at a given reaction temperature T. RF_{CH4} is the response factor of the CH_4 gas determined by external calibration. Please note that S_{CO2} represents the utilization of O_2 towards CO_2, whereas S_{CH4} describes the portion of converted CO appearing as CH_4.

2.3 Structural and morphological characterization

Temperature-programmed reduction (H_2-TPR) profiles were recorded in an automated catalyst characterization system (Micromeritics, model AutoChem II), which incorporates a thermal conductivity detector (TCD). 50 mg of the sample was loaded in a U tube and heated by 5 °C·min^{-1} under 10mL·min^{-1} of 10% H_2 in Ar. Ex situ XRD patterns were collected on a Bruker D8 advance diffractometer using Cu Kα radiation. The crystallite size of cobalt phase was calculated according to the line broadening of the most intense reflections using the Scherrer's equation

[48]. The BET specific surface area of Co-Mn based materials was determined by N_2 physisorption measurements, while Kr-BET was used for pure CoO for higher precision measurements due to the extremely low surface area. Samples were degassed at 200 °C for 5 h before launching the adsorption-desorption of N_2. The specific surface areas were calculated according to the Brunauer–Emmett–Teller (BET) method using data points in the relative pressure (p/p0) range of 0.05–0.35. Scanning Transmission electron microscopy (STEM) analysis of calcined, reduced and spent $CoMn_8O_x$ catalysts was carried out using a JEOL 2100 FEG S/TEM microscope operated at 200 kV equipped with a spherical aberration corrector on the probe forming lens. The samples were dispersed by ultrasonication in ethanol and deposited on a holey carbon coated TEM grids. The STEM images were carried out using a spot size of 0.13 nm, a current density of 140 pA and a camera focal length of 8 cm, corresponding to inner and outer diameters of the annular detector of about 73 and 194 mrad. Elemental analyses of Co, Mn and O were carried out with an EDX probe using a silicon drift detector (SDD) with a sensor size of 60 mm^2. The morphology of fresh and spent catalysts was examined by a Zeiss GeminiSEM 500 SEM microscope, combining with energy dispersive X-ray spectroscopy (EDX) to study the distribution of elements on surface.

2.4 Synchrotron-based *in situ* spectroscopic study

Synchrotron-based *in situ* NAP-XPS and NEXAFS experiments were performed at CAT branch of the EMIL beamlines (Energie Materials In-situ Laboratory Berlin) at the synchrotron radiation facility BESSY II of the Helmholtz Zentrum Berlin [49,50]. Two catalysts (pure CoO_x and Co_8MnO_x) were examined under identical conditions on a comparative basis. The powder catalysts were pressed into pellets and mounted on the sample holder using a stainless-steel mask. The sample stage was heated from the back side by an IR laser and the temperature was measured by a K-type thermocouple attached to the sample surface. The gasses were introduced *via* four calibrated mass flow controllers (Bronkhorst) and the total flow rate was kept constant at 15 $mL \cdot min^{-1}$. The COPrOx mixture composition was: 1%CO, 1%O_2 and 50%H_2 in He and the total pressure was kept at 0.5 mbar. The gas phase composition was monitored by a differentially pumped quadrupole mass spectrometer (QMS, Pfeiffer PrismaPro), which was connected to the experimental cell through a leak valve. Unfortunately, the gas phase signal changes during reaction were minor and unfit for analysis. The entrance of the electron analyzer lenses was of cone-shape (nozzle) ending with a 1 mm diameter hole. The sample/nozzle distance during NAP-XPS measurements was kept around 2 mm. The Co 2p and Mn 2p spectra were recorded using specific photon energies, so that the collected photoelectrons have the same kinetic energy (240 or 560 eV) allowing similar sample information depths (ca. 2 and 3.5 nm, respectively). The NEXAFS Co L_3-edge and Mn L_3-edge peaks were measured in the total electron yield (TEY) mode.

Given the possibility that Mn oxides might be reduced by the synchrotron radiation, Mn 2p spectra have been recorded twice at different time spans of the experiment. The similarity of the spectra suggests that the oxidation state of Mn is not affected by the continuous exposure to the X-ray beam.

2.5 Operando NAP-XPS study using a monochromatic AlKα X-ray source

The *operando* NAP-XPS study of pure CoO_x, Co_8MnO_x and $CoMn_8O_x$ catalysts was performed at Charles University in Prague, Czech Republic. The experiments were carried out on a photoelectron spectrometer (SPECS Surface Nano Analysis GmbH, Germany) which is equipped with a PHOIBOS-150 multichannel hemispherical electron energy analyzer coupled with a differentially pumped electrostatic pre-lens system. Spectra were obtained using the monochromatized Al Kα X-ray source (1486.6 eV). The powder of fresh as-synthesized catalysts was pressed to pellets and fixed on the sample holder using a stainless-steel mask with a window at the top. The thermocouple was welded on the mask at the side which was in contact with the sample surface. The catalyst was investigated in 1.3 $mL \cdot min^{-1}$ flow of pure H_2, pure O_2 and in a COPrOx feed with the $CO:O_2:H_2$ molar ratios of 1:1:98 (note, He was not co-feed in this experiment). Before introduction of the COPrOx gases, the sample was pre-reduced in 1 mbar H_2 at 400°C for about 2 hours. After cooling down to 50 °C, the COPrOx mixture was introduced into the NAP-XPS cell and the pressure stabilized to 1 mbar. The XPS spectra were collected after 30 min in each temperature. Similar to synchrotron-based NAP-XPS the entrance of the photoelectrons to the lenses was via a nozzle, but in this case the entrance hole diameter was much smaller (0.3 mm) which allows a distance between sample and nozzle of the same value. The entrance of the electron analyzer lenses was of cone-shape (nozzle) ending with a 1 mm diameter hole. The sample/nozzle distance during NAP-XPS measurements was kept around 2 mm. The gas phase in the cell was monitored by a QMS (Pfeiffer PrismaPro) fitted in the 1st pumping stage of the analyzer pre-lenses.

2.6 In situ NEXAFS at 1bar under model redox conditions

The Co_8MnO_x sample was analyzed in 1 bar of H_2 and O_2 by NEXAFS at the APE-HE beamline of the Elettra synchrotron radiation facility (Trieste, Italy), using a dedicated reaction cell described in detail elsewhere [51]. The NEXAFS signal was detected in TEY mode, by probing the drain current from the sample with a picoammeter. The gases were introduced in the reaction cell via calibrated mass flow controllers keeping a constant gas flow of 50 $mL \cdot min^{-1}$. Initially the sample was treated in O_2 at 200 °C for 15 min and subsequently cooled down under He gas flow. In situ NEXAFS spectra at Co and Mn L_3-edges were recorded at selected temperatures in the 38-300 °C range first in 100% H_2 and then in 10% O_2/He. NEXAFS data were acquired after 15 min at each selected temperature point. Data treatment, involving energy alignment, background subtraction

using an asymmetric least square fitting routine and normalization to the total area under the curves, was performed by using the recently developed THORONDOR code [52]. The relative concentration of each oxidation state was calculated based on linear combination fit (LCF) analysis using as reference NEXAFS spectra of model Co and Mn oxides obtained from previous experiments[42] or from the literature [53]. LCF was carried out using the ATHENA program [54], for the experimental *in situ* NEXAFS data at Co and Mn L_3-edge, pretreated in THORONDOR. LCF errors on the retrieved relative fractions of each component are estimated to be ±5%.

2.7 Uncertainties in the comparison of spectroscopic results between different setups

This paper discus *in situ*/operando spectroscopic results collected in the 3 different spectrometers. Evidently in an *in situ* spectroscopic experiment, the analysis chamber of the spectrometer also serves as a catalytic cell. As described above the design of each setup is quite distinct, likely influences the reaction conditions in each experiment. One can mention here the difference in the cell volume, possible offset in the temperature reading due to the position of the thermocouple and the type of heating (laser or resistive heater), the flow of the reactants and their dilution or not in He. All these differences complicate the comparison of the results between different spectrometers and can explain for example the relatively stable CoO phase in the laboratory NAP-XPS tests as will be shown below. Notably, the COPrOx reactants flow has a clear effect on the reactivity and the surface oxidation state of cobalt as will be discussed in a future publication [55]. One should note that the QMS signal response in the laboratory-based NAP-XPS experiment was better as compared to the synchrotron-based NAP-XPS described above. Since the two setups use the same QMS, the reason behind this difference is most likely related to the particular reaction conditions applied in the two NAP-XPS spectrometers. These include the pressure (0.5 against 1 mbar), the contact time between the catalyst and the gas phase (linked with the setup design, the volume of the reactor/cell, the size of the pellet, the flow rate, *etc.*) and definitely the installation position of the QMS in the two instruments.

2.8 Peak fitting and quantitative analysis of XPS spectra

The Co 2p spectra were fitted using standard reference curves of metallic Co, CoO and Co_3O_4 recorded at the same spectrometer. The full width at the half maximum and the energy difference between the three reference peaks were fixed during fitting. The reference peaks were allowed to vary until the difference between their sum and the experimental spectra (residual standard deviation, STD) was minimized (typically between 1 and 2). The procedure was repeated two times using different initial and final background positions as well as linear and spline-linear backgrounds (this is justified since reference peaks and spectra on the catalysts were not necessarily have the same background profiles). The error bars in the quantification of the different cobalt oxidation states represents the STD of the two fitting approaches by the mean

value. The deconvolution of the Mn 2p peak is more challenging owing to the similarities of the various peaks corresponding to each Mn phase. However, by superimposing two Mn 2p spectra small differences were distinguished due to the divergence in the peak position and width (of about 0.2-0.3 eV) of the various manganese oxidation states. To enhance the robustness of the peak fitting procedure, four different approaches were used for Mn 2p peak deconvolution. These fitting approaches involved peak profiles of reference Mn components or by using 6 individual Gaussian/Lorentzian (GL) peaks, as well as different types of background subtraction (linear or Shirley type) [56]. The Mn oxidation state given in this paper is the mean value of the four deconvolution processes and the error bar corresponds to the maximum deviation among the four approaches. The Mn 2p profile between synchrotron, and laboratory-based NAP-XPS setups, was very similar (see Figure S1) which validates the utilization of the same deconvolution procedure of the Mn 2p spectra in the two experiments. In this way, any error in the estimation of the relative amount of the Mn^{2+}, $Mn^{3+}$and Mn^{4+} should be systematic and consistent throughout this study. Quantitative analysis of elements was performed using normalized intensities and, for synchrotron-based photoemission studies, the photon flux and energy dependence of the atomic subshell photoionization cross sections [57] were taken into account. The XPS Co 2p and Mn 2p peak intensities were simulated using SESSA vs.2.1.1 software [58] for model consisting of MnO_2 particles supported on planar CoO substrate. Three MnO_2 particle morphologies (cubes, hemispheres and regular pyramids with square base) and five particle sizes (from 1.5 nm to 0.5μm height) were modelled. The density of the particles on the support was left to vary up to the point where the simulated Co 2p and Mn 2p peak area ratio converged with the experimental one.

3 Results

3.1 Textural and morphological properties of CoO_x/MnO_x

The X-ray diffraction patterns recorded before (fresh after calcination) and after reduction are presented in Figure S2. The pattern of fresh CoO_x corresponds to the single CoO phase (JCPDS 03-065-2902), but after reduction two types of metallic cobalt phases were found. The stronger diffraction peaks come from the face-centred cubic phase (fcc; JCPDS 15-0806) and the weaker from hexagonal phase (hcp; JCPDS 05-0727) [59]. As far as the calcined Co_8MnO_x is concerned, all the observed peaks are attributed to Co_3O_4 (JCPDS 03-065-3103), without any traces of Mn-containing phases. The absence of Mn-related peaks might be due to low crystallinity and high dispersion of Mn. However, after reduction in addition to metallic cobalt, small amounts of MnO are seen in the diffraction patterns. On the fresh $CoMn_8O_x$ sample, Co_3O_4-like phases are not observed and the most intense peaks are characteristic of a hausmannite phase (Mn_3O_4, JCPDS 01-089-4837) while small peaks indicate the presence of ramsdellite (MnO_2, JCPDS 01-073-

1539). After reduction, only characteristic peaks of the MnO phase (JCPDS 07-0230) are detected implying reduction of MnO_2 and Mn_3O_4 phases.

The specific surface area of the three catalysts as measured after the reduction pretreatment at is shown in Table 1. The CoO_x catalyst has the lowest surface area of 1.4 m^2g^{-1}, while in case of Co_8MnO_x and $CoMn_8O_x$ the surface area is 6.5 to 8.5 m^2 g^{-1}, respectively. The crystallite size estimated from the XRD patterns based on Scherrer's equation is included in the same table. The smaller crystallite size of Co^0 in Co_8MnO_x samples (please note that the same CoO_x particles were also used for Co_8MnO_x synthesis) suggests that the growth of metallic cobalt nanoparticles is somewhat limited by the addition of Mn. An alternative explanation could be a significant contribution of manganese oxide, since in general oxide phases have higher BET surface area than metals.

Table 1. Textural parameters of reduced Co-based catalysts.

Catalyst	***S_{BET} (m^2 g^{-1})***	***Crystallite size[a] (nm)***
	Reduced	***Reduced***
CoO_x	1.4	32.7 (Co^0)
Co_8MnO_x	6.5	26.8 (Co^0), 23.2 (MnO)
$CoMn_8O_x$	8.5	23.0 (MnO)

a. The crystallite size of each major phase was estimated from the Scherrer's equation applied to the most intense diffraction peak.

H_2-TPR measurements were conducted with the aim to compare the bulk reducibility of each catalyst. As shown in Figure S3 for the calcined pure CoO_x sample two main peaks are observed: one relatively sharp at 275 °C and a broader one centered around 365 °C. The two peaks are usually attributed to the progressive reduction of Co_3O_4 *via* a two-step reduction process (Co_3O_4 → CoO → Co) [42]. The TPR profile of the Mn-rich catalyst ($CoMn_8O_x$) is dominated by peaks related to the progressive reduction of manganese oxide (MnO_2 → Mn_3O_4 → MnO) in accordance with literature reports [44,60]. In particular, the peaks at 270 °C and 440 °C correspond to MnO_2 and Mn_3O_4 reduction, respectively. Note that the reduction peaks of cobalt oxides are not clearly evidenced in this sample due to the relatively low amount of cobalt and the strong overlapping between its reduction peaks with those of the manganese oxides. However, a broad peak is observed in the high temperature region (near 550 °C) which cannot be attributed to neither of the single MnO_x or CoO_x phases and may be caused by synergetic interactions between Mn and Co species. This assignment is also supported by the TPR profile of the Co_8MnO_x catalyst showing

a clear shift of the reduction peaks to the high-temperature region, the more intense of which is centered at around 500 °C. The shift in the reduction temperature has been attributed before to the formation of a $Co_{3-x}Mn_xO_4$-type solid solution upon calcination [60–63], as expected according to the phase diagram of Co-Mn-O system [64] and previous experimental studies [65–67]. However the absence of any relevant diffraction lines in the XRD data suggest that mixed Co-Mn-O phases either do not form at all in our catalyst or are structurally disordered or nanosized enough, to escape detection by XRD.

The morphology of CoO_x, Co_8MnO_x and $CoMn_8O_x$ catalysts after calcination and reduction pretreatment was examined by SEM (Figure S4). All three catalysts form big aggregates which are composed of fine particles clearly distinguished in most of the SEM micrographs. The particle size of CoO_x and Co_8MnO_x range between 50 and 200 nm, while in the case of $CoMn_8O_x$ (Figure S4c) the particles seem larger. After reduction at 400 °C, the particle size of both catalysts significantly increased. The images recorded after reduction of Co_8MnO_x clearly evidence a sintering process, with a rougher surface as compared to its previous form. The EDX analysis of large surface areas of the Co_8MnO_x catalyst after calcination gave a Mn/Co ratio of around 1/10 (Figure S5), which is close to the nominal value (0.125) used during synthesis. Similar Mn/Co ratios were also found after analysis of individual spots on the surface, indicating that initially Mn is homogenously distributed over the cobalt surface. Interestingly, after the reduction pretreatment the EDX analysis of several spots revealed important differences in the Mn/Co ratios. In particular, depending on the analysis spot the Mn/Co ratio can vary from 0.11 to 0.7. In addition, the spots with high Mn/Co ratios are always accompanied by high oxygen content.

Details about the microstructure of Co_8MnO_x catalyst were acquired by STEM combined with EDX analysis. STEM-EDX maps of several aggregates after H_2 pretreatment and COPrOx reaction (spent catalyst) are presented in Fig. 1a and b, while those of the fresh-calcined catalyst can be found in Figure S6. The red and green color areas in the figure indicate Co- and Mn-enriched areas, respectively. Elemental mapping confirms the significant inhomogeneity of the grains after reduction, shown in larger scale by SEM-EDX, which is preserved without large variations also at the spent catalyst. In particular, in some sample areas Mn is well dispersed over Co particles, while in others Mn and Co areas are clearly separated. A common feature which is visible in several of the STEM-EDX images in Fig. 1 is that Mn content is increasing at the edge of the particle, suggesting that Mn is enriched on the surface of the grains. However, several other areas also exist where Co signal extents up to the perimeter of the aggregate revealing uncovered/exposed cobalt surface. The % Mn and Co atomic concentration as calculated from the EDX signal of each image are included as pie charts in Fig. 1. The large variation of %Mn from 5 to 17% between the various micrographs evokes the significant variation Mn distribution over

Co particles. This implies that Mn is not equally distributed over cobalt but it is segregated to form Mn-rich areas on the surface of Co_8MnO_x sample, at least after reducing pretreatment.

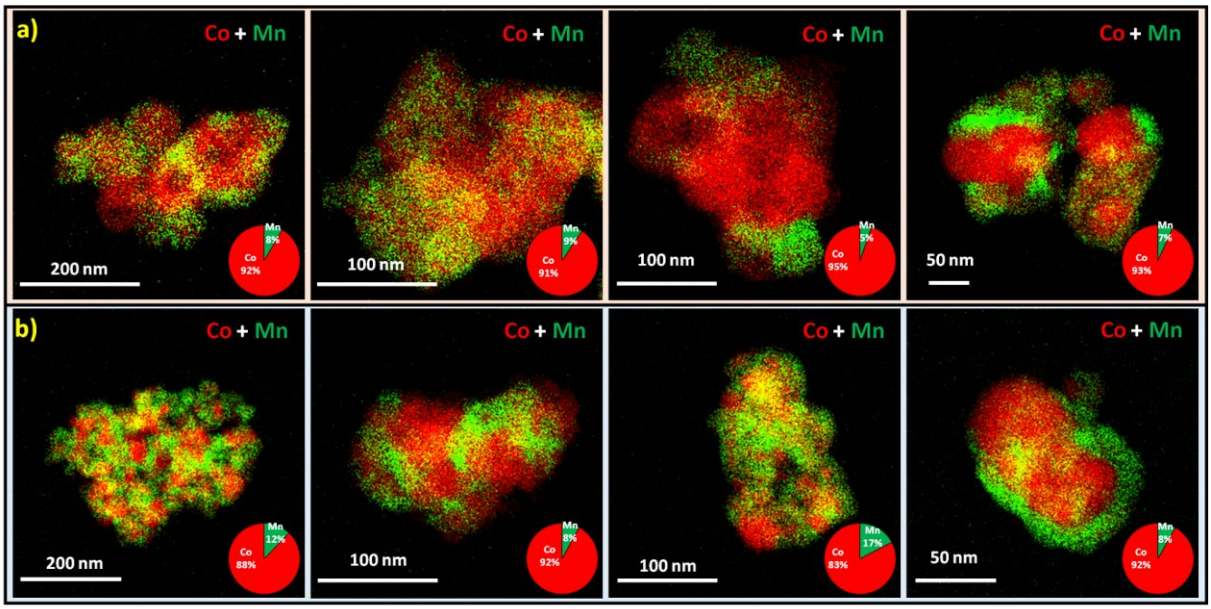

Figure 1. STEM-EDX analysis images with elemental mapping (merged Co+Mn) collected over several Co_8MnO_x catalyst aggregates after **a)** reduction at 400 °C in 1 bar H_2 for 30 min and **b)** spent catalyst after 6h reaction in 1 bar COPrOx at temperatures up to 350 °C. Red and green color areas correspond to Co- and Mn-enriched areas, respectively. The % atomic concentration of Mn and Co is presented in the pie charts at the right-bottom side of each panel.

3.2 Fixed-bed reactor catalytic tests

The reactivity of the three catalysts after H_2 reducing pretreatment was evaluated in a fixed-bed reactor. The CO conversion (X_{CO}) starts at 150 °C and increases sharply above this temperature for all catalysts (Figure 2a), with the Co_8MnO_x having systematically higher X_{CO} than the other two. The differences are quite remarkable at intermediate temperatures, with more than 98% of CO conversion over Co_8MnO_x at 250 °C and only 51 and 29% for pure CoO_x and $CoMn_8O_x$, respectively. A small decrease from 98% to 96% of X_{CO} is observed for Co_8MnO_x above 250 °C. The O_2 conversion (X_{O2}) is the overall consumption of O_2 for both CO and H_2 oxidation (eq. 1 and 2, respectively). Please note here, that since the catalyts were pretreated in a reducing environment prior to the reaction, O_2 may also have been consumed to oxidize the pre-reduced cobalt, in addition to eq. 1 and 2. As shown in Figure 2b, at 200 °C the Co_8MnO_x catalyst converts more O_2 than the other two but above this temperature the X_{O2} is stable at 95% for all catalysts. The selectivity towards CO_2 (S_{CO2}, Figure 2c) represents the O_2 utilization for CO oxidation to CO_2 (eq. 1). Up to 200 °C, the S_{CO2} of Co_8MnO_x and CoO_x catalysts are very similar, while above this temperature Co_8MnO_x seems to be more selective than CoO_x. The $CoMn_8O_x$ catalyst has significantly lower S_{CO2} than the other two, which means that excess Mn promotes H_2 oxidation (eq. 2). Finally, the selectivity of CO to CH_4 (S_{CH4}) shown in Figure 2d increases significantly at

250 °C, showing that at higher temperatures CO hydrogenation (eq. 3) is promoted. The CH_4 production path via CO_2 hydrogenation (eq. 4) cannot be excluded completely, but it is less probable since CO is relatively easy to hydrogenated as compared to CO_2 at the same reaction conditions [68].

CO oxidation: $CO + ½\ O_2 \rightarrow CO_2$ (1)

H_2 oxidation: $H_2 + ½\ O_2 \rightarrow H_2O$ (2)

CO hydrogenation: $CO + 3\ H_2 \rightarrow CH_4 + H_2O$ (3)

CO_2 hydrogenation: $CO_2 + 4\ H_2 \rightarrow CH_4 + 2\ H_2O$ (4)

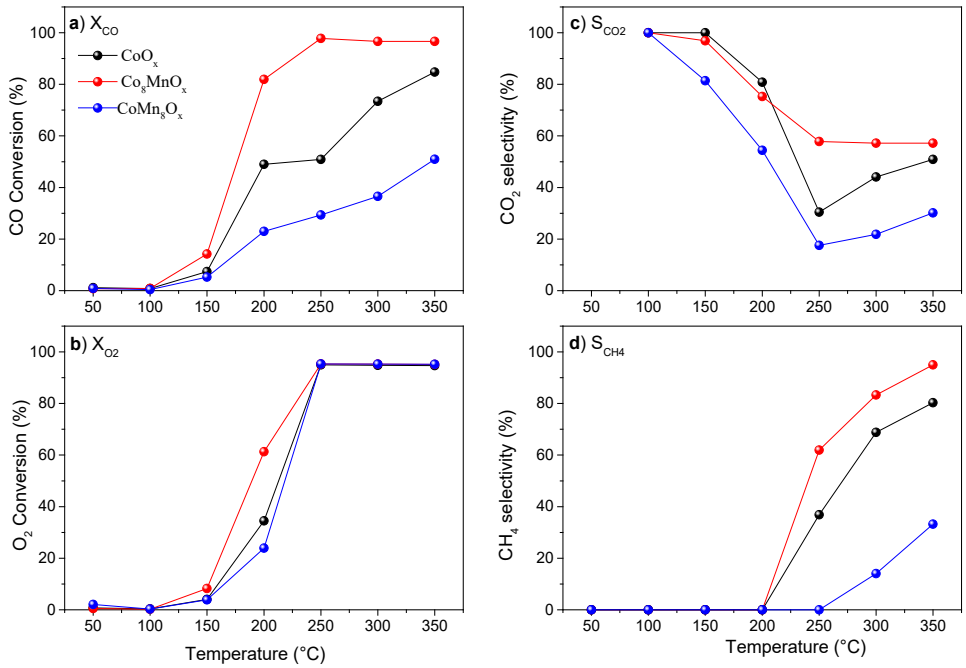

Figure 2. COPrOx activity tests. a) CO conversion, b) O_2 conversion and c) CO_2 selectivity d) CH_4 selectivity *vs.* temperature, over pure CoO_x (●), Co_8MnO_x (●) and $CoMn_8O_x$ (●) catalysts. Experimental conditions: 1% CO, 1% O_2, and 50% H_2 in He-balanced flow; 0.05 g of catalyst; 50 mL min^{-1} of total flow; atmospheric pressure (1 bar). Every data point was recorded after 30 min equilibration at each temperature.

3.3 In situ surface characterization of the Co-Mn by *synchrotron* NAP-XPS and NEXAFS

The catalytic results suggest that addition of small amounts of Mn on CoO improves the activity and the selectivity towards CO_2, but excess of Mn (i.e. in the $CoMn_8O_x$ catalyst) is detrimental for the COPrOx reaction. In this paragraph *in situ* NAP-XPS and NEXAFS are used to compare the Co_8MnO_x and CoO_x surface oxidation state and composition under reaction conditions. The Co_8MnO_x catalyst was selected due to its superior performance as compared to $CoMn_8O_x$. The reactants feed, in the synchrotron-based NAP-XPS and NEXAFS experiments at 0.5 mbar, was identical to the one of the fixed-bed reactor tests at 1 bar. The discussion focus on the

stability of Co and Mn under COPrOx environment and the fix-bed reactor tests are used as benchmark of the reactivity.

3.3.1 Comparison of the cobalt oxidation state between the two catalysts

Figure 3a displays the Co $2p_{3/2}$ spectra recorded on pure CoO_x after H_2 pretreatment and during the COPrOx reaction. Metallic cobalt (Co^0) formed under pretreatment in H_2, undergoes progressive oxidation during COPrOx reaction. The evolution of cobalt oxidation state was calculated by deconvolution of the Co 2p peak using reference spectra and is presented in Figure 3e. When the reaction temperature reaches 250 °C, more than 80% of cobalt has been converted to CoO. Then, within a short period of time at 250 °C, CoO undergoes further oxidation to Co_3O_4 and remains stable after that to a mixed Co_3O_4/CoO=70/30 state. The Co L_3-edge NEXAFS recorded after 1 h and 2 h at 250 °C under COPrOx conditions are shown together with reference CoO and Co_3O_4 spectra (in green dotted line)[69] in Figure 3b. During COPrOx the Co L_3-edge has a maximum at 780.5 eV and a shoulder located at 778.5 eV, resembling the Co_3O_4 reference spectrum. However, it can be noticed that the intensity ratio between the 780.5 eV and 778.5 eV peaks is different in the two cases. This difference, together with the small peak feature at 777.5 eV, marks the presence of cubic rocksalt CoO with Co^{2+} in octahedral position (O_h, see the reference in green dotted line) [42]. Consequently, both NAP-XPS and NEXAFS spectra of pure CoO_x catalyst at 250 °C in COPrOx underline a mixed state between Co_3O_4 and CoO species.

In case of the Co_8MnO_x catalyst the Co $2p_{3/2}$ peak and the derived cobalt oxidation state, shown in Figure 3c, indicate some evident differences from CoO_x. In particular, after the H_2 pretreatment the catalyst is not totally reduced, and, in general, Co_8MnO_x catalyst contains more CoO. Similar conclusions can be also drawn from the NEXAFS spectra shown in Figure 3d. The surface stability of Co_8MnO_x catalyst was examined at 350 °C and as shown in Figure 3c, after 30 min at this reaction temperature metallic Co reappears in the spectrum at the expense of Co_3O_4, while longer reaction times (about 1 h at 350 °C) favors progressive re-oxidation to Co_3O_4. Surprisingly the amount of CoO is not considerably influenced by the raise in the temperature and remains similar around 50% at both temperatures. At 350 °C the Co L_3-edge peak shape is modified as compared to 250 °C indicating a mixture of Co-CoO-Co_3O_4, in full accordance with the NAP-XPS results.

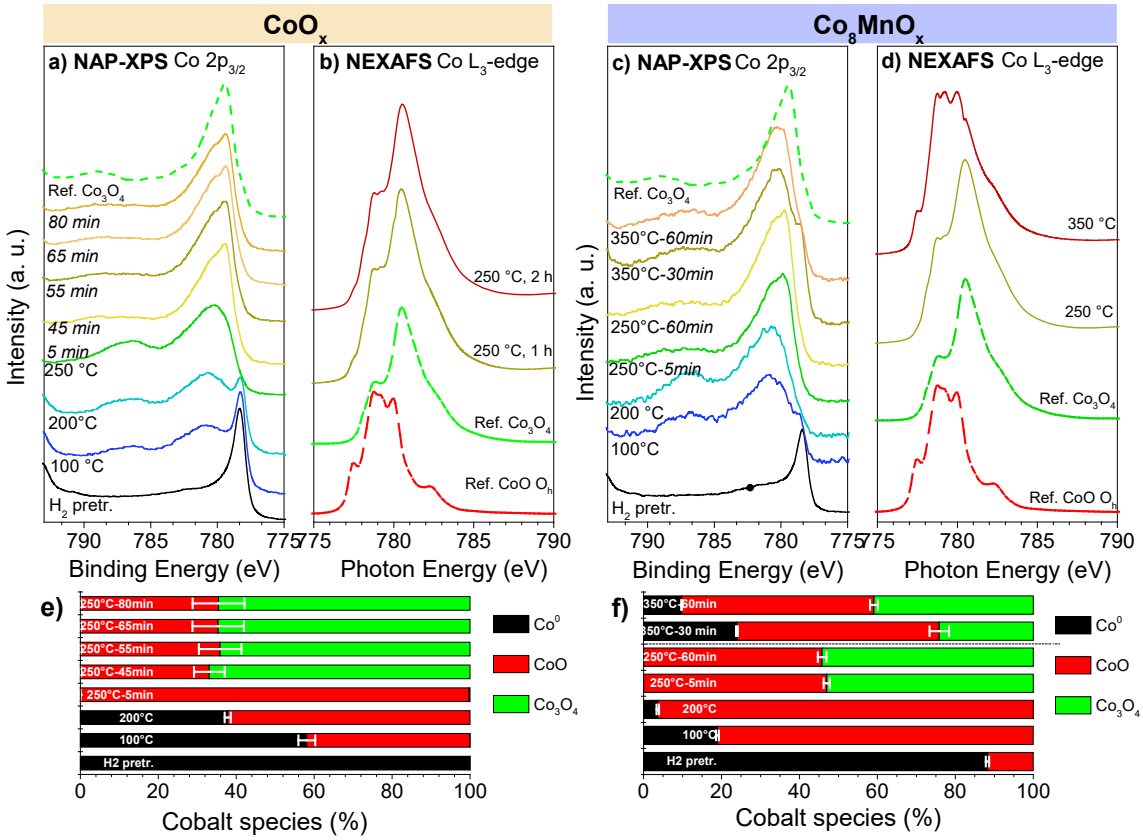

Figure 3. In situ NAP-XPS and NEXAFS spectra of a,c) Co $2p_{3/2}$ (hv = 1020 eV) and b,d) Co L_3-edge recorded on pure CoO_x (a,b) and Co_8MnO_x (c,d) after H_2 pretreatment and during COPrOx at various temperatures. Operating conditions: 0.5 mbar of 1% CO, 1% O_2, 50% H_2 and He, from room temperature to 250 °C. The bar graphs e) and f) show the percentage of each cobalt oxidation state calculated by deconvolution of the relevant Co 2p peaks.

3.3.2 Analysis of the Mn oxidation state and distribution

The manganese oxidation state is discussed next. The NAP-XPS Mn $2p_{3/2}$ and NEXAFS Mn L_3-edge spectra are shown in Figures 4a and b respectively. The distribution of Mn oxidation states (Figure 4c) was estimated by deconvolution of the Mn 2p peaks. In accordance with several works devoted to Mn curve fitting [70–72], the peaks of Mn^{2+} (MnO) and Mn^{3+} (Mn_2O_3) appear at very similar BEs (around 641 eV), but the peak of MnO is followed by a characteristic shake-up satellite at 647.5 eV, which allows distinguishing the two oxidation states.The Mn^{4+} state (MnO_2) has similar peak profile with respect to Mn^{3+} but is shifted by 1 eV to higher BEs. The different oxides can be distinguished better by their Mn L_3-edge NEXAFS spectra which show distinctly different features [53].

During H_2 pretreatment manganese is reduced to the lowest oxidation state observed in this work, which is Mn^{2+}. This is quite evident also by the satellite feature at the Mn 2p photoelectron peak and the similarity of the Mn L_3-edge NEXAFS spectra with that of MnO reference (green dotted line). Mn^{2+} was progressively oxidized to Mn^{3+} and M^{4+} during the heating step to 250 °C

under the COPrOx feed. However, at 350 °C part of Mn^{4+} reduces back to Mn^{3+}/Mn^{2+} states as also confirmed by the Mn L_3-edge, matching reasonably well the Mn_3O_4 spinel oxide (or $MnO{\cdot}Mn_2O_3$). This redox behavior is similar to the one observed for cobalt, i.e. oxidation up to 250 °C and partial reduction at higher temperature, showing that temperature and gas phase composition define the redox ability of the gas phase.

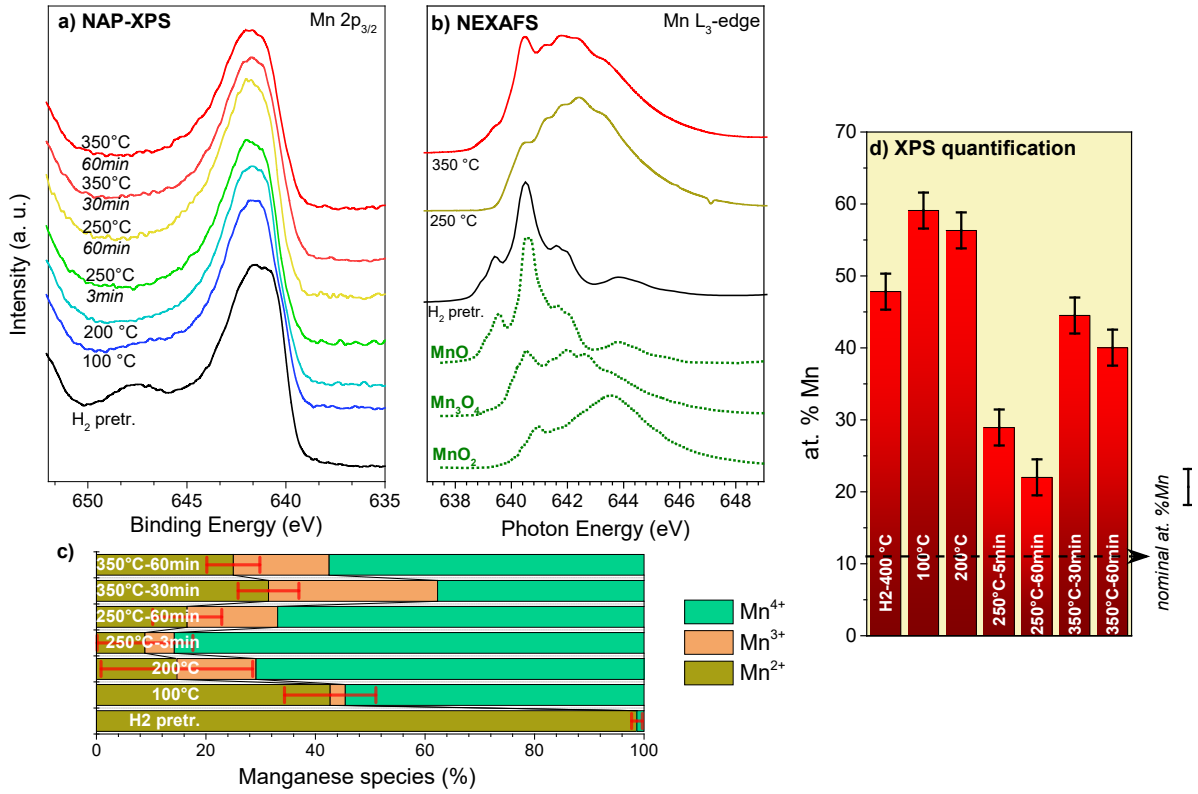

Figure 4. In situ NAP-XPS and NEXAFS spectra of a) Mn $2p_{3/2}$ (hv = 880 eV) and b) Mn L_3-edge recorded on Co_8MnO_x at room temperature, after H_2 pretreatment and during COPrOx at various temperatures. Reference Mn L_3-edge spectra were retrieved from reference [53]. Operating conditions: 0.5 mbar of 1% CO, 1% O_2, 50% H_2 balance He, from room temperature to 250 °C and 350 °C. c) Bar graph showing the percentage of each Mn oxidation state calculated by deconvolution of the Mn 2p peaks shown in (a). d) The evolution of Mn concentration (metal at. %) at various reaction conditions calculated from the Mn 2p and Co 2p NAP-XPS spectra. The estimated analysis depth to be 2.2±0.1 nm.

The Mn/(Mn+Co) atomic ratio (hereafter at. %Mn) shown in Figure 4d was calculated based on Mn 2p and Co 2p spectra. Four excitation photon energies, corresponding to two analysis depths (or information depths) were used (see Table S1). It is clear that for all the temperatures examined here the surface concentration of Mn is much higher than the 12% nominal value. A significant drop of %Mn is observed at 250 °C in the COPrOx, while at 350 °C the %Mn rises back again. Comparison of the two analysis depths (Table S1) reveals that the %Mn is systematically higher at the most surface sensitive mode (around 2.2 nm), which means that Mn is mainly segregated over cobalt. This suggests no extensive mixed oxide phase formation, in agreement with the XRD results discussed above.

3.4 Redox stability of Co_8MnO_x measured by *in situ*–NEXAFS at 1bar

The NAP-XPS and NEXAFS results identified the oxidation states of cobalt and manganese that are involved in the COPrOx reaction providing some useful insights of the reactivity in the fixed-bed reactor experiments. However, the relatively low operating pressure (0.5 mbar) of NAP-XPS raises same doubts about the extrapolation of the redox behavior of the catalyst at atmospheric pressure conditions. To clarify this point we performed *in situ* NEXAFS experiments at 1 bar on Co_8MnO_x under reducing (100% H_2) and oxidizing (10% O_2/He) atmospheres [51]. Figure 5 shows the Co L_3-edges (a,b) and Mn L_3-edges (c,d) of calcined Co_8MnO_x upon annealing in H_2 and subsequently in 10% O_2/He. The relative concentration of each oxidation state, estimated by linear combination fit analysis, is included in the right part of each graph. Initially the Co L_3-edge corresponds to the Co_3O_4 oxide (Fig. 5a) while reduction to about 50% of CoO is observed at 250 °C. The Mn L_3-edge after calcination (Fig. 5c) resembles to the one of MnO_2, but in H_2 this phase reduces gradually to Mn_3O_4 (at 200 °C) and MnO (at 250 °C).

Exposure of the pre-reduced Co_8MnO_x to 10%O_2 (Fig. 5b and d) initiates a gradual oxidation of MnO to MnO_2 and CoO to Co_3O_4. Notably, oxidation of MnO is facile since the catalyst is transformed to a mixture of Mn_2O_3/MnO_2 already at 50 °C, while at 100 °C more than 70 % of manganese has been oxidized to MnO_2. In 10% O_2, both cobalt and manganese are more oxidized as compared to the COPrOx mixture investigated with NAP-XPS. This is expected from the more oxidizing gas feed of 10%O_2. Nevertheless, the aforementioned NEXAFS results suggest that the mixed oxidation states found at the surface of Co_8MnO_x catalyst in the 0.5 mbar NAP-XPS experiment can be maintained even at atmospheric pressure.

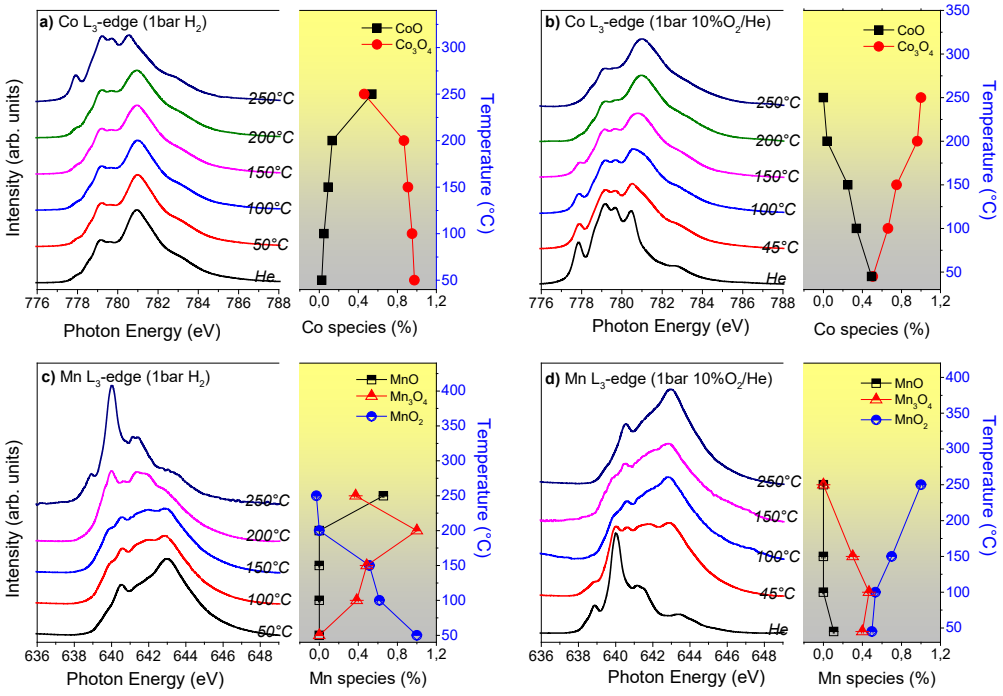

Figure 5. *In situ* Co L_3-edge NEXAFS spectra of Co_8MnO_x catalysts recorded at a) 1 bar H_2 and b) 1 bar 10%O_2 in He between 50-250°C. The corresponding Mn L_3-edge is shown in c) and d), respectively. The evolution of the different Co and Mn oxidation states/phases estimated by linear combination fit analysis using reference spectral profiles of relevant Co- and Mn-oxides are included in the right part of each graph. this is not the case here.

3.5 Operando *AlKα source* NAP-XPS measurements

In this paragraph cobalt catalysts (Co, Co_8MnO_x and $CoMn_8O_x$) with identical oxidation states are compared with or without Mn addition, in order to distinguish the Mn effect on the COPrOx selectivity. As described in the experimental part the reaction conditions are different from those of the synchrotron-based experiments having notable effect on cobalt oxidation state. After the H_2 pretreatment at 400 °C, the surface of pure CoO_x was fully reduced to Co^0 while that of the Mn-based catalysts remained as CoO. This difference is consistent with the findings of H_2-TPR measurements (Fig. S3) showing that Mn addition shifts CoO_x reduction at higher temperatures. However, in this case CoO resists more to reduction as compared to synchrotron-based NAP-XPS reactor (Fig. 3c and 3f).

Figure 6 displays the Co $2p_{3/2}$ peaks of the three catalysts recorded in COPrOx at three characteristic temperatures. For pure CoO_x, the intense peak at 778.4 eV due to Co^0 [73] converts to broad peak at 780.6 eV with a shake-up satellite peak at 786.3 eV, characteristic of Co^{2+} [74], indicating a progressive oxidation of Co^0 to CoO (Figure 6d). On the contrary, in the case of Co_8MnO_x and $CoMn_8O_x$ catalysts, cobalt remains as CoO at all reaction temperatures. The analysis of the Mn $2p_{3/2}$ peaks taken from the two Mn-containing catalysts (Fig. S7), shows that Mn is progressively oxidized but remains always in a mixed $MnO/Mn_2O_3/MnO_2$ state. A comparison between the two Co-Mn samples show that Co_8MnO_x promotes Mn^{2+} and Mn^{4+} while $CoMn_8O_x$ favor more Mn^{3+} species.

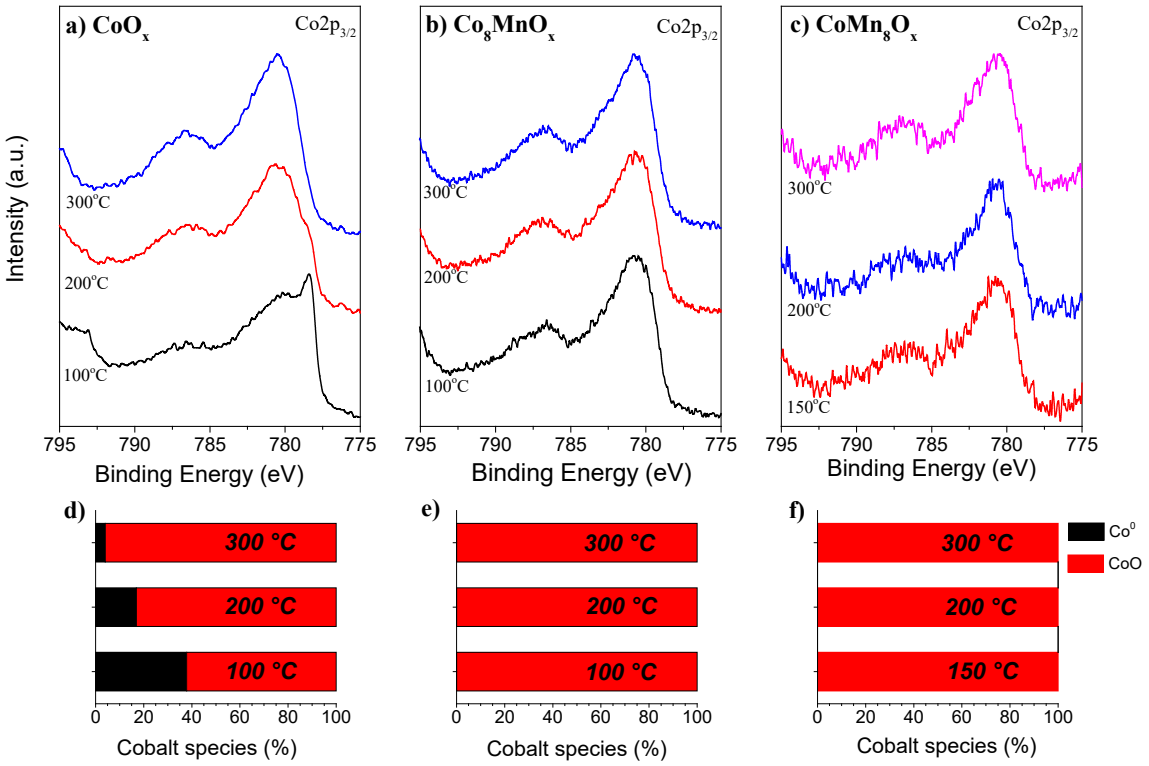

Figure 6. In situ NAP-XPS spectra of Co 2p$_{3/2}$ on a) pure CoOx, b) Co$_8$MnO$_x$ and c) CoMn$_8$O$_x$ recorded during COPrOx at various temperatures. The distribution of cobalt species resulting from Co 2p$_{3/2}$ peak analysis is shown in the bar plots: (d,e and f) below of each set of spectra. Operating conditions: 1 mbar of 1% CO, 1% O_2 and 98% H_2, from room temperature to 300 °C.

The X_{CO} and X_{O2}, as well as the S_{CO2} and S_{CH4} calculated by the QMS signal are shown in Figure 7. In all cases the CO and O_2 conversion (Figures 7a and 7b) appears from around 100 °C and increase at higher temperature. The X_{CO} of Co$_8$MnO$_x$ and CoO$_x$ catalysts are alike up to 250°C, while for CoMn$_8$O$_x$ it is significantly lower (Figure 7a). A similar trend is also observed in the S_{CO2} (Figure 7c), with CoMn$_8$O$_x$ having the lowest S_{CO2} of the three catalysts, while those of Co$_8$MnO$_x$ and CoO$_x$ are comparable. The selectivity of CO to CH_4 (S_{CH4}, Figure 7d), is practically zero up to 150 °C, but above this temperature for CoO$_x$ rises, most notably at 300 °C. This implies boost of hydrogenation reactions (eq. 3 and 4) and explains the high X_{CO} of CoO$_x$ at 300 °C (Figure 7a). Clearly for this sample CO is consumed via methanation reaction (eq. 3) at 300 °C while the Co$_8$MnO$_x$ catalyst becomes more selective to H_2O as expected at this temperature region.

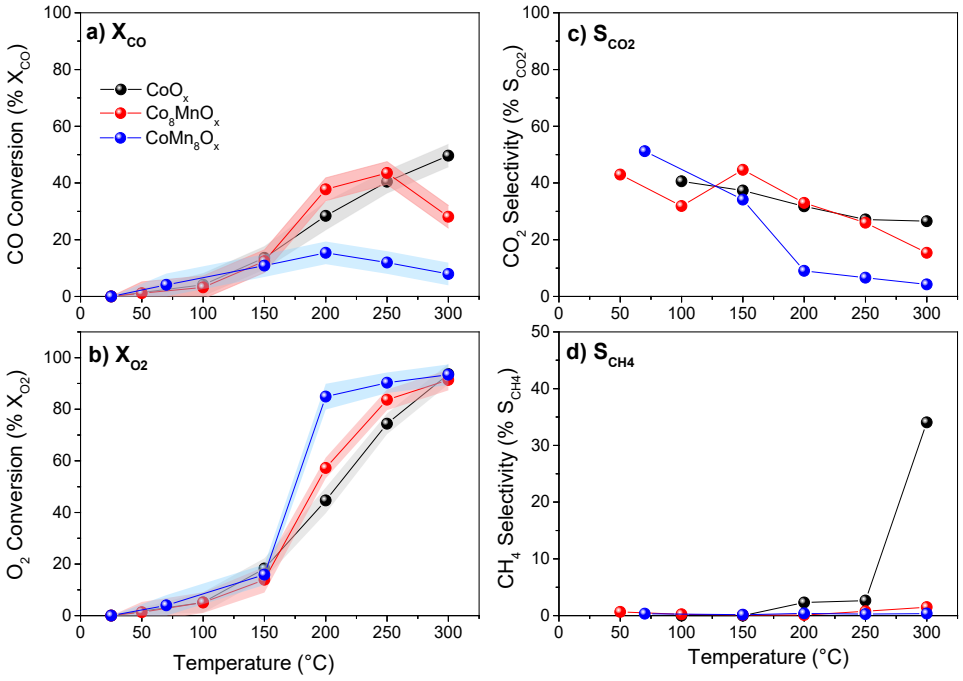

Figure 7. Conversion of *(a)* CO (X_{CO}) and *(b)* O_2 (X_{O2}). The selectivity of *(c)* O_2 to CO_2 (S_{CO2}) and *(d)* CO to CH_4 calculated from *on line* mass spectrometry data recorded on pure CoO_x (●) Co_8MnO_x (●) and $CoMn_8O_x$ (●) during NAP-XPS measurements under COPrOx conditions. Prior to the activity tests, the samples were pretreated in the XPS chamber under 1 mbar of H_2 at 400 °C for 1 h.

3.5 Effect of Mn-Co nanoscale spatial distribution on Co oxidation state during COPrOx

NAP-XPS suggested that CoO and Co_3O_4 states coexist on the surface of the Co-Mn catalysts under operation. In addition the SEM-EDX analysis in Figure S5 as well as the STEM-EDX in Figure 1, implies a significant diversity at the Co_8MnO_x morphology, with some areas having higher Mn concentration than others. Here we try to understand if these two characteristics are connected, in an attempt to understand the reason of the enhanced CoO stability observed on Co-Mn catalysts. The discussion will be focused on the Co_8MnO_x catalyst since is the one which shows the better catalytic performance.

The surface area analyzed by the employed synchrotron-based NAP-XPS setup is largely defined by the spot size of the incident X-ray beam, as the electron collecting cone of the analyzer is much larger than 1 mm. Under the current working conditions the X-ray spot on the sample is a parallelogram with dimensions of 180x10 μm^2. The small area spot analysis of synchrotron-based NAP-XPS can be used to provide details regarding the effect of Mn on the oxidation state of cobalt. To do so, NAP-XPS spectra were collected in two different spots of the catalyst pellet, by shifting the sample lateral position with respect to the analyzer, while keeping the sample at the same reaction conditions (250 °C in COPrOx). In this way we could directly detect the oxidation state of cobalt in areas that are rich or poor in Mn and draw conclusions about possible Mn effect over the redox stability of cobalt oxides.

The Co 2p spectra recorded at two characteristic sample positions are shown in Figure 8. The first (*spot 1*) with high Mn concentration, and a second (*spot 2*) with low Mn concentration. For comparison the results presented in Figure 3 are collected in the position of spot 1. Based on Co 2p peak deconvolution it becomes evident that CoO concentration is higher in areas that contain more Mn *(spot 1)*, while Co_3O_4 prevails in areas dominated by cobalt *(spot 2)*. In particular, the CoO/Co_3O_4 from 44/56 in Mn-rich area of the catalyst drops to 30/70 in the Co-rich area. Please note that the 30/70 ratio coincides with that observed for the parent pure CoO_x. The CoO/Co_3O_4 ratio in the two spots is practically the same for the two analysis depths (not shown), which means that there is no depth distribution between CoO and Co_3O_4 and within the outer 4 nm the two cobalt oxides are homogeneously mixed.

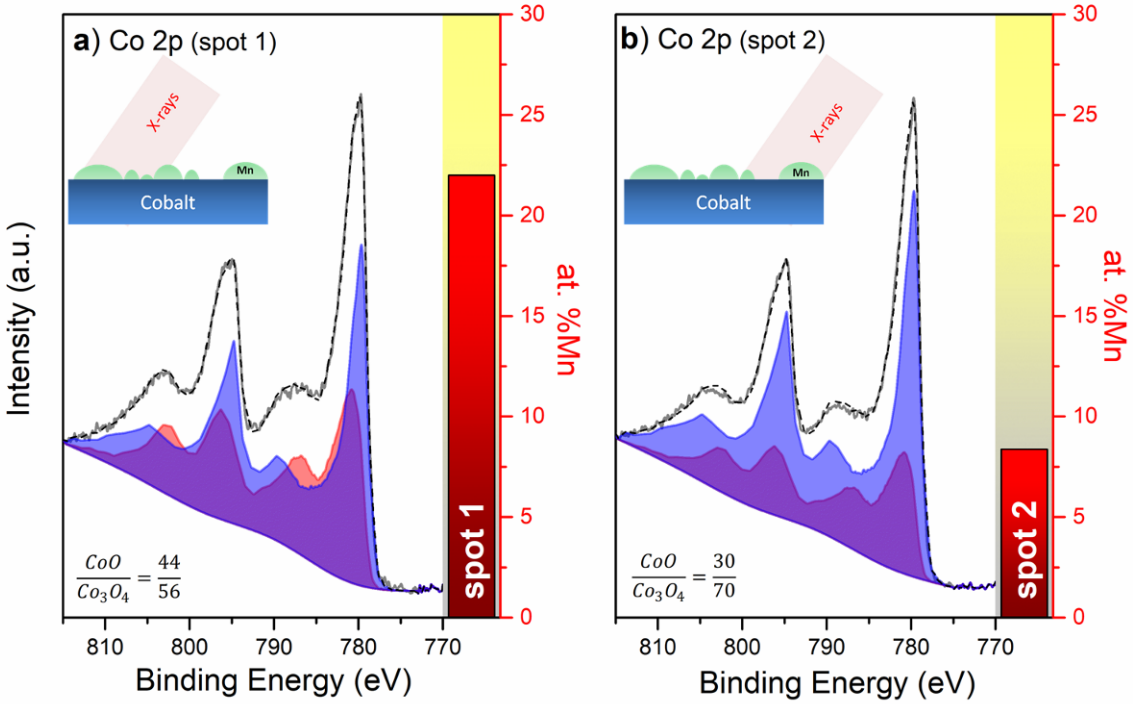

Figure 8. The Co 2p spectra recorded over two different areas (spots) of Co_8MnO_x catalyst under identical COPrOx reaction conditions. Each Co 2p peak was deconvoluted into CoO (dark purple peak) and Co (light purple peak) components. The bar in the right part of each figure shows the at. % Mn calculated by the Mn 2p and Co 2p peaks recorded at each spot. A schematic representation of the expected morphology in each spot based on the % Mn is included at the top-left of each figure.

The effect of Mn on Co oxidation state in areas were the two elements are in close proximity is addressed by high resolution STEM (HRSTEM). The inhomogenuity of Co_8MnO_x catalyst can be used as an opportunity to examine, at the same aggregate, uncovered and Mn-overlapping Co areas at nanoscale level. The STEM-EDX images can serve as a guide to identify the two areas on an aggregate. Figure 9 presents HRSTEM images of spent Co_8MnO_x catalyst, collected in areas

exclusively occupied by Co, as manifested by the STEM-EDX image shown in the left-up panel. Similar images taken in other Co_8MnO_x aggregates can be found in Figure S8. The interplanar spacing (lattice fringes) of 0.24 nm measured in area 1 (marked by white lines) corresponds to Co_3O_4 (311) lattice planes. The presence of Co_3O_4 is confirmed by the Fast Fourier transform (FFT) diffraction pattern of a selected area (area 3), clearly show characteristic diffraction spots due to the different Co_3O_4 lattice planes.

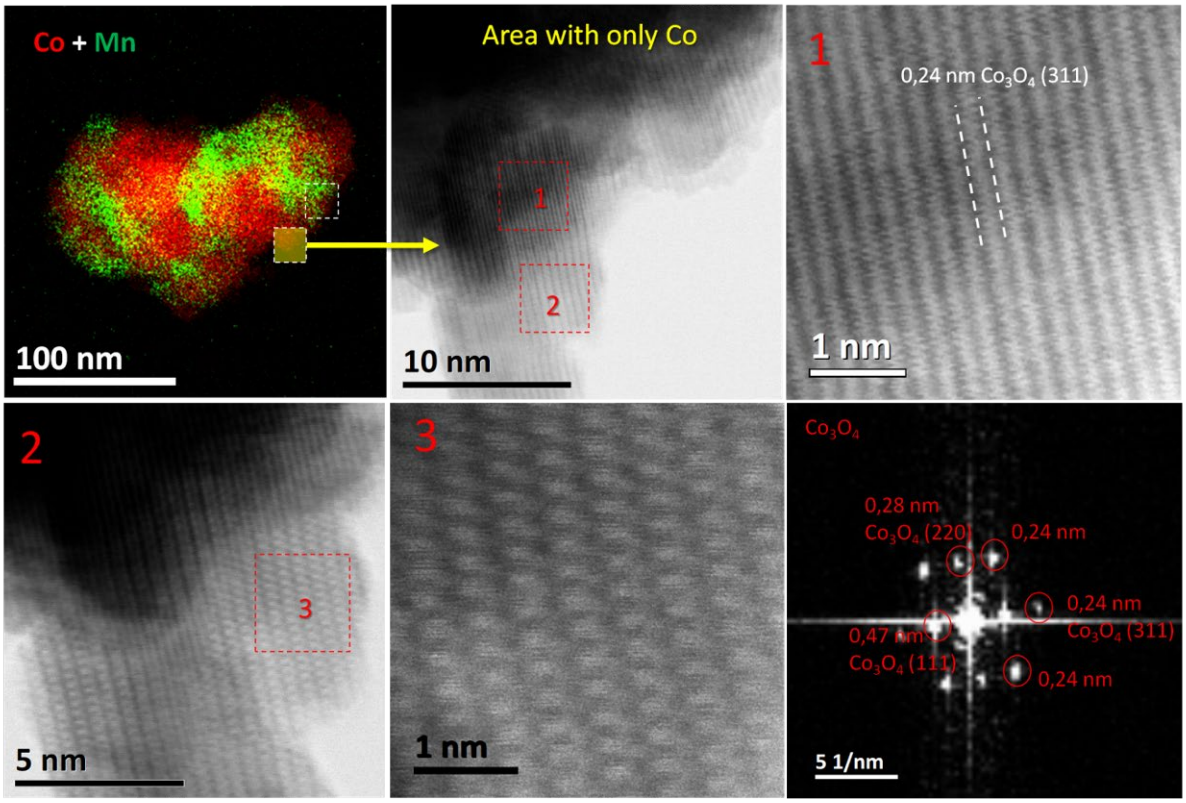

Figure 9. STEM-EDX (top left) image of the spent Co_8MnO_x catalyst and the high resolution bright field STEM images derived from catalyst areas composed *exclusively by cobalt*. The interplanar spacing is indicated by two parallel lines. The squares indicate the part of the low magnification image from which the high-resolution images are derived. The FFT diffraction pattern at the bottom-right corresponds to spot 3 besides.

Similar analysis was also carried out in aggregate areas where overlapping between Co and Mn signals was indicated by STEM-EDX analysis. Figure 10 shows HRSTEM images and FFT patterns recorded in such an area. More HRSTEM images from overlapping Co and Mn areas can be found in Figures S9. The images taken at the Co and Mn interface area evoke a border between the two oxide phases indicated in the image by a red line. The measurements of the lattice fringes, well resolved at the HRSTEM images taken at the two sides of this border, are consistent with MnO or MnO_2 and CoO, respectively. The presence of CoO in the vicinity with manganese oxide is evidenced also in the FFT patterns taken in the same area. Analysis of other aggregates presented in Figure S9, suggest that stabilization of CoO phase in areas close to Mn is a general feature of the Co_8MnO_x sample in complete accordance with NAP-XPS results of Figure 8.

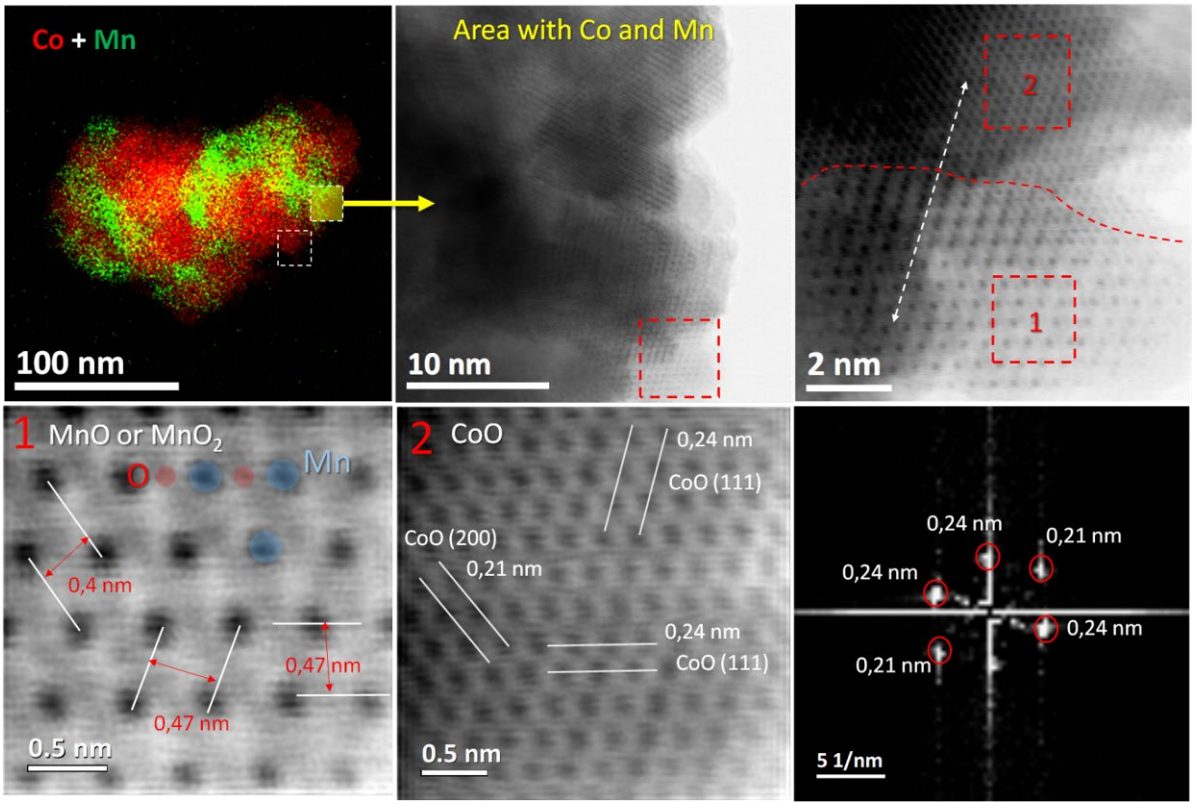

Figure 10. STEM-EDX (top left) image of the spent Co_8MnO_x catalyst and the high resolution bright field STEM images derived from catalyst areas where *Co and Mn overlap*. The interplanar spacing is indicated by two parallel lines. The squares indicate the part of the low magnification image from which the high-resolution images are derived. The Mn and O atoms of MnO or MnO_2 are displayed in blue and red respectively and are superpositioned on the image. The FFT diffraction pattern at the bottom-right corresponds to image besides.

The correlation between Mn excess and higher CoO concentration implies that Mn helps to stabilize the CoO phase at conditions where pure cobalt tents to oxidize to Co_3O_4 (e.g. Figure 3a and 3b). Based on our previous results [42] CoO is far more active than Co_3O_4 for COPrOx. Therefore, partial stabilization of CoO over Co_8MnO_x catalyst is expected to enhance the activity of this catalyst as compared to pure cobalt, in addition to the its effect on maintain the surface area indicated by BET. However, STEM-EDX and SEM-EDX images manifest that there are areas on the Co_8MnO_x surface where cobalt is not in contact with Mn. These areas are expected to preserve the redox properties of the parent material (i.e. CoO_x), therefore being prone to oxidation to Co_3O_4 and to reduction towards Co^0, at low and high COPrOx reaction temperature, respectively.

We discus now about the possible CoO stabilization mechanism in areas close to manganese. HRSTEM images clearly show that the lattice fringes close to the Co-Mn interface corresponds well to those of the individual metal oxides. There is no evidence of formation of a new mixed phase at their interface, for example a mixed Co-Mn oxide. On a macroscopic scale, formation of mixed Co-Mn oxide may be detected by the shift of the Co 2p satellite peak [75]. Comparison of

the Co $2p_{3/2}$ spectra between Co_8MnO_x and CoO_x samples in cases where Co^{2+} is the dominant oxidation state (see Figure S10) do not reveal any evident difference in the shake-up satellite peak position in our case (around 786.8 eV). Besides, the Co L-edge NEXAFS spectra of the two samples are also similar (see Fig. 3b and d). Therefore, the similarities of both XPS and NEXAFS spectra between the two catalysts, together with the HRSTEM and XRD analysis results discussed above, suggest that Mn and Co do not form a mixed Co-Mn oxide phase but form rather separated oxides in close proximity. Therefore stabilization of CoO should be attributed phenomena taking place at the interface during reaction, as for example facile exchange of O^{2-} ions, which cannot be detected here.

4 Discussion

The catalytic tests at 1 bar showed that the addition of Mn on Co (Co_8MnO_x) promotes the COPrOx activity and CO_2 selectivity. On the other hand, Co_8MnO_x has relatively high CH_4 selectivity in the reaction. At this point we will try to elucidate the role of the manganese promotion on cobalt reactivity by synthesizing the results presented above. Before doing that we should highlight two different paths in which Mn may influence the reactivity. The first is related to the the partial stabilization of the CoO phase with beneficial effects on the catalytic activity and O_2 selectivity to CO_2 [42]. We consider this path as an *indirect effect* of Mn on the reactivity in the sense that Mn stabilizes CoO, but it is the oxidization state of cobalt that determines the reactivity. The second path considers that Mn influences the reactivity by directly participating in the reaction, independently of its effect on the cobalt oxidation state. To distinguish the two paths we will call this *direct effect* of Mn on the reactivity. For conciseness, the discussion is mainly based on the comparison between CoO_x and Co_8MnO_x since these catalysts are derived from the same CoO nanopowder.

The role of manganese on the COPrOx activity

BET surface area measurements after reduction indicate that addition of Mn on cobalt enhances the thermal stability giving almost 4.5 times higher specific surface area for Co_8MnO_x than that of pure CoO_x. In general, higher surface areas should lead to better reactivity, providing that the increase in the exposed surface atoms is proportional to the increase in the number of the active catalytic sites. The surface analysis results presented above makes clear that the cobalt atoms reside in a variety of states and environments (e.g. oxidation states, contact with Mn atoms *etc.*). There are also solid evidences [42] that each cobalt state exhibits different catalytic activity in the given reaction, which renders the quantification of the surface active sites problematic on our powder catalysts. Nevertheless, the best possible approximation to compare the reactivity of pure and Mn-promoted Co catalysts remains to normalize the conversion to the

total number of the exposed Co atoms (i.e. surface area). However, although for pure CoO_x the BET surface area coincides with the exposed Co atoms, in case of Co_8MnO_x both Mn and Co sites are counted. Besides, as shown by STEM-EDX and NAP-XPS, the majority of Mn is segregated over Co reducing its accessibility to the reactants.

Unfortunately it is not possible to measure directly the uncovered surface area of cobalt on Co_8MnO_x catalyst, but quantitative simulation of the XPS peak intensities can help to get an approximate estimation of this number. In order to minimise the effect of the inhomogeneity in the surface distribution of Mn over Co (see Fig. 8) the Co_8MnO_x was measured after reducing, oxidizing and UHV annealing treatments using a dual anode X-ray source with analysis area of 12x12 mm^2. These measurements gave an average $R_{Mn}=\frac{Mn\ 2p}{Mn\ 2p+Co\ 2p}$ ratio of 0.19±0.1. The quantitative simulations of Mn 2p and Co 2p peaks using SESSA vs 2.1.1 software (see supporting information 10) concluded that for Co_8MnO_x the experimental R_{Mn} corresponds to about 24% of exposed/uncovered cobalt area as compared to the overall surface of the catalyst. Consequently, and according to the BET measurements shown in table 1, the specific surface area of exposed cobalt atoms over Co_8MnO_x catalysts is around 1.6 m^2g^{-1} (the rest 4.9 m^2g^{-1} of the surface is covered by Mn). Although this is a rough estimation, it suggests that the differences in the X_{CO} of the two catalysts (Fig. 2a) are not justified just on the grounds of their surface area differences.

Thus, differences in the cobalt oxidation state between pure and Mn-promoted cobalt catalysts, clearly shown in Fig. 3, remain a plausible scenario to explain their activity. This can be exploited further by comparing the qualitative differences between Co_8MnO_x and CoO_x in the catalytic tests of Fig. 2 (1 bar) and Fig. 7 ($1x10^{-3}$ bar). In particular, at 1 mbar the X_{CO} is similar for the two catalysts (Fig. 7a), but it is very different at 1 bar (Fig. 2a). NAP-XPS shows that at 1 mbar CoO dominates both CoO_x and Co_8MnO_x catalysts and as expected [42], similar cobalt surface states give comparable X_{CO} in Fig. 7. In contrast, at 1 bar, the surface state of the two catalysts is different as anticipated by synchrotron NAP-XPS (Fig. 3), with CoO_x catalyst favoring Co_3O_4 formation. High amounts of Co_3O_4 have a negative effect [42] on the X_{CO} of CoO_x catalyst, rationalizing a lower activity than the $CoMn_8O_x$ in Fig. 2a. The argument above point to the fact that Mn-promotion effect on X_{CO} is mainly related to the stabilization of CoO state and there is no indication that manganese is directly benefits the COPrOx reactivity. Therefore, the previously reported high MnO_x activity for CO oxidation [43] seems not to be preserved in H_2 presence.

The role of manganese on the COPrOx selectivity

After discussing the effect of Mn on the activity, we turn now our attention to the COPrOx product selectivity. We recall here that the desired product of COPrOx reaction is CO_2, but there

are two other by-products of the reaction, namely H_2O and CH_4, which should be avoided since their formation consumes valuable H_2. Therefore, a selective COPrOx catalyst should boost the production of CO_2 and minimize that of H_2O and CH_4. We continue to use arguments based on the the catalytic tests of Fig. 2 (1 bar) and Fig. 7 ($1x10^{-3}$ bar) to address the selectivity issue. A notable difference among 1 mbar and 1 bar catalytic tests is in the S_{CO2}. More specifically in Fig. 2 the S_{CO2} of Co_8MnO_x is distinctly higher than CoO_x while in Fig. 7 their differences are marginal. As discussed above, the higher S_{CO2} of Co_8MnO_x observed at 1 bar test is compatible with the higher amount of CoO on this catalyst. The similarity of S_{CO2} in the two catalysts at 1 mbar experiment is consistent with the fact that the oxidation state of cobalt is the same for both (i.e. CoO). This observation suggests that that the addition of small Mn quantities on cobalt does not have direct effects on the S_{CO2}. However, in Mn excess (i.e. $CoMn_8O_x$ catalyst), both 1 mbar and 1 bar catalytic tests implies that the undesired H_2 oxidation reaction is promoted (Eq. 2) leading to the formation of water. This is supported by the *operando* NAP-XPS measurements, which show distinct differences in the S_{CO2} between Co_8MnO_x and $CoMn_8O_x$, especially above 200 °C, while in both catalysts the surface is dominated by CoO (Fig. 6). Therefore, it appears that in COPrOx, manganese oxides are much more active for H_2 oxidation than CO oxidation.

Another difference between the results of Figures 2 and 7 is noticed in the selectivity of CO to CH_4 (S_{CH4}). In particular, at 1 bar the Co_8MnO_x has higher S_{CH4} than CoO_x while at 1 mbar the reaction trend among the two catalysts is reversed. CH_4 is produced by the methanation/hydrogenation of CO and/or CO_2 according to eq. 3 and 4. Methanation reactions are known to be more effective with temperature and by the presence of reduced cobalt (Co or CoO) [11]. This can explain why in 1 bar tests, S_{CH4} of Co_8MnO_x is higher since this catalyst has also higher proportion of CoO. However, at 1 mbar, where the surface of both catalysts is dominated by CoO, only pure CoO_x catalyst shows the expected high S_{CH4}, while for Co_8MnO_x the S_{CH4} is about 20 times lower. This result indicates that Mn helps to suppress CO methanation reactions on CoO and most probably moderates the S_{CH4} at 1 bar, which without its addition could be even higher. This argument is in line with the absence of any CH_4 in case of $CoMn_8O_x$ catalyst (Fig. 7c). Although the mechanism via which Mn influences the CH_4 selectivity cannot deduced from our studies, its influence on CH_4 selectivity, together with the structural stability are the only *direct effects* of Mn on the cobalt reactivity (the others are being related to the stabilization of CoO state).

Overall, we have shown that Mn-promotion helps to stabilize the CoO phase and, in this way, enhances the COPrOx activity. However, the interaction of Co and Mn is rather weak and their segregation is facilitated either during pre-treatment or under reaction conditions. A direct effect of this, is that in parts of the catalyst where Mn and Co are not in contact, Co_3O_4 is readily formed

under reaction conditions with negative effects on the CO conversion and S_{CO2} selectivity. Most probably, more complex synthesis methods than the impregnation or co-precipitation used in this work, could be elaborated to enhance the distribution of Mn on Co and stabilize the CoO phase, targeting to a more active and selective Co-Mn catalyst. However, the significant evolution of the Mn surface concentration under reaction conditions (Fig. 4d), suggests that, in long term, stability might be an issue for Co-Mn catalysts. In addition to that, a commercially viable cobalt-based COPrOx catalyst should employ relatively simple synthesis methods, like those used in this work, which can scale-up easily. Therefore, the effort to enhance the stability of CoO in cobalt-based COPrOx catalysts should be pursued, possibly by testing other promoters with higher synergy with cobalt.

5 Conclusions

In this work Mn-Co catalysts were synthesized and their performance in COPrOx reaction was evaluated. The addition of Mn on Co (Co_8MnO_x) led to a significant increase of the catalyst performance. NAP-XPS indicates that the CoO phase is partially stabilized in the presence of Mn, leading to higher catalytic activity. Depending on the operating conditions (time, temperature, gas mixture, etc.), MnO can be progressively oxidized into MnO_2 and reduced back to MnO. Excess of MnO_x on the catalyst's surface was correlated with high O_2 consumption through the unwanted H_2 oxidation. Although, Mn addition helps to stabilize the CoO phase promoting the catalytic activity, the synergy of the two metals is limited by segregation and aggregation of Mn over Co surface. The dynamic transformation of the surface oxidation state and composition during COPrOx reaction was directly evident in the spectroscopic studies under working conditions. Thus, to the authors opinion further efforts are needed in order to fabricate promoted cobalt-based catalysts able to stabilize the CoO phase on their surface for sufficiently long reaction periods.

Acknowledgments

LZ and DKC would like to thank the China Scholarship Council (CSC) for supporting their studies at ICPEES. MB acknowledges financial support from Strasbourg University via the IdEX-2018 (Post-doctorants) project. EB and DHL acknowledge the support from PRIN-2017 MOSCATo, project n. 2017KKP5ZR. We thank Prof. C. Petit for the useful and constructive discussions, as well as Dr. T. Dintzer for the SEM-EDX measurements. L. Braglia, A. Martini, D. Salusso and M. Signorile are acknowledged for their help during the in situ NEXAFS data collection on APE-HE and, with R.K. Shrestha, subsequent data treatment. We are also grateful to P. Torelli and G. Ricchiardi for their support during the measurements at APE-HE, as well as insightful discussions and advices. The authors acknowledge the CERIC-ERIC Consortium for the access to Near Ambient Pressure XPS@Charles University in Prague and financial support. Finally, we acknowledge HZB for the allocation of synchrotron radiation beamtime and ALBA Synchrotron staff for the collaboration during the experiments.

6 References

[1] P. Jing, X. Gong, B. Liu, J. Zhang, Recent advances in synergistic effect promoted catalysts for preferential oxidation of carbon monoxide, Catal. Sci. Technol. 10 (2020) 919–934. doi:10.1039/c9cy02073j.

[2] D.I. Potemkin, E.Y. Filatov, A. V. Zadesenets, A.M. Gorlova, N.A. Nikitina, D.A. Pichugina, A comparative study of CO preferential oxidation over Pt and Pt0.5Co0.5 nanoparticles: Kinetic study and quantum-chemical calculations, Mater. Lett. 260 (2020) 126915. doi:10.1016/j.matlet.2019.126915.

[3] L. Cao, W. Liu, Q. Luo, R. Yin, B. Wang, J. Weissenrieder, M. Soldemo, H. Yan, Y. Lin, Z. Sun, C. Ma, W. Zhang, S. Chen, H. Wang, Q. Guan, T. Yao, S. Wei, J. Yang, J. Lu, Atomically dispersed iron hydroxide anchored on Pt for preferential oxidation of CO in H2, Nature. 565 (2019) 631–635. doi:10.1038/s41586-018-0869-5.

[4] N. Bion, F. Epron, M. Moreno, F. Mariño, D. Duprez, Preferential oxidation of carbon monoxide in the presence of hydrogen (PROX) over noble metals and transition metal oxides: Advantages and drawbacks, Top. Catal. 51 (2008) 76–88. doi:10.1007/s11244-008-9116-x.

[5] Y.H. Kim, S.D. Yim, E.D. Park, Selective CO oxidation in a hydrogen-rich stream over Ru/SiO 2, Catal. Today. 185 (2012) 143–150. doi:10.1016/j.cattod.2011.07.022.

[6] B. Qiao, J. Liu, Y.G. Wang, Q. Lin, X. Liu, A. Wang, J. Li, T. Zhang, J. Liu, Highly Efficient Catalysis of Preferential Oxidation of CO in H2-Rich Stream by Gold Single-Atom Catalysts, ACS Catal. 5 (2015) 6249–6254. doi:10.1021/acscatal.5b01114.

[7] K. Liu, A. Wang, T. Zhang, Recent Advances in Preferential Oxidation of CO Reaction over Platinum Group Metal Catalysts, ACS Catal. 2 (2012) 1165–1178. doi:10.1021/cs200418w.

[8] S.S. Maluf, E.M. Assaf, CO preferential oxidation (CO-PROx) on La1 - XCe xNiO3 perovskites, Catal. Commun. 12 (2011) 703–706. doi:10.1016/j.catcom.2010.12.022.

[9] J. Ding, L. Li, H. Li, S. Chen, S. Fang, T. Feng, G. Li, Optimum Preferential Oxidation Performance of CeO2-CuOx-RGO Composites through Interfacial Regulation, ACS Appl. Mater. Interfaces. 10 (2018) 7935–7945. doi:10.1021/acsami.7b15549.

[10] A. Elmhamdi, R. Castañeda, A. Kubacka, L. Pascual, K. Nahdi, A. Martínez-Arias, Characterization and catalytic properties of CuO/CeO2/MgAl2O4for preferential oxidation of CO in H2-rich streams, Appl. Catal. B Environ. 188 (2016) 292–304. doi:10.1016/j.apcatb.2016.02.011.

[11] Y. Teng, H. Sakurai, A. Ueda, T. Kobayashi, Oxidative removal of co contained in hydrogen by using metal oxide catalysts, Int. J. Hydrogen Energy. 24 (1999) 355–358. doi:https://doi.org/10.1016/S0360-3199(98)00083-4.

[12] C.S. Polster, H. Nair, C.D. Baertsch, Study of active sites and mechanism responsible for highly selective CO oxidation in H2 rich atmospheres on a mixed Cu and Ce oxide catalyst, J. Catal. 266 (2009) 308–319. doi:10.1016/j.jcat.2009.06.021.

[13] Y. Yoshida, Y. Izumi, Recent Advances in the Preferential Thermal-/Photo-Oxidation of Carbon Monoxide: Noble Versus Inexpensive Metals and Their Reaction Mechanisms, Catal. Surv. from Asia. 20 (2016) 141–166. doi:10.1007/s10563-016-9216-8.

[14] C. Tang, J. Sun, X. Yao, Y. Cao, L. Liu, C. Ge, F. Gao, L. Dong, Efficient fabrication of active CuO-CeO2/SBA-15 catalysts for preferential oxidation of CO by solid state impregnation, Appl. Catal. B Environ. 146 (2014) 201–212. doi:10.1016/j.apcatb.2013.05.060.

[15] A. Davó-Quiñonero, M. Navlani-García, D. Lozano-Castelló, A. Bueno-López, J.A. Anderson, Role of Hydroxyl Groups in the Preferential Oxidation of CO over Copper Oxide-Cerium Oxide Catalysts, ACS Catal. 6 (2016) 1723–1731. doi:10.1021/acscatal.5b02741.

[16] J.S. Elias, N. Artrith, M. Bugnet, L. Giordano, G.A. Botton, A.M. Kolpak, Y. Shao-Horn, Elucidating the Nature of the Active Phase in Copper/Ceria Catalysts for CO Oxidation, ACS Catal. 6 (2016) 1675–1679. doi:10.1021/acscatal.5b02666.

[17] X. Xie, Y. Li, Z.Q. Liu, M. Haruta, W. Shen, Low-temperature oxidation of CO catalysed by Co3O4 nanorods, Nature. 458 (2009) 746–749. doi:10.1038/nature07877.

[18] M. Khasu, T. Nyathi, D.J. Morgan, G.J. Hutchings, M. Claeys, N. Fischer, Co3O4 morphology in the preferential oxidation of CO, Catal. Sci. Technol. 7 (2017) 4806–4817. doi:10.1039/c7cy01194f.

[19] Z. Zhao, M.M. Yung, U.S. Ozkan, Effect of support on the preferential oxidation of CO over cobalt catalysts, Catal. Commun. 9 (2008) 1465–1471. doi:10.1016/j.catcom.2007.12.013.

[20] Z. Zhao, X. Lin, R. Jin, Y. Dai, G. Wang, High catalytic activity in CO PROX reaction of low cobalt-oxide loading catalysts supported on nano-particulate CeO2-ZrO2 oxides, Catal. Commun. 12 (2011) 1448–1451. doi:10.1016/j.catcom.2011.05.031.

[21] T.M. Nyathi, N. Fischer, A.P.E. York, D.J. Morgan, G.J. Hutchings, E.K. Gibson, P.P. Wells, C.R.A. Catlow, M. Claeys, Impact of Nanoparticle–Support Interactions in Co 3 O 4 /Al 2 O 3 Catalysts for the Preferential Oxidation of Carbon Monoxide , ACS Catal. 9 (2019) 7166–7178. doi:10.1021/acscatal.9b00685.

[22] I. Czekaj, J. Wambach, O. Kröcher, Modelling Catalyst Surfaces Using DFT Cluster Calculations, (2009) 4310–4329. doi:10.3390/ijms10104310.

[23] Z. Zhao, R. Jin, T. Bao, X. Lin, G. Wang, Mesoporous ceria-zirconia supported cobalt oxide catalysts for CO preferential oxidation reaction in excess H2, Appl. Catal. B Environ. 110 (2011) 154–163. doi:10.1016/j.apcatb.2011.08.038.

[24] L.E. Gómez, I.S. Tiscornia, A. V. Boix, E.E. Miró, Co/ZrO2 catalysts coated on cordierite monoliths for CO preferential oxidation, Appl. Catal. A Gen. 401 (2011) 124–133. doi:10.1016/j.apcata.2011.05.007.

[25] T.M. Nyathi, N. Fischer, A.P.E. York, M. Claeys, T. M. Nyathi, N. Fischer, A. P. E. York, M. Claeys, Environment-Dependent Catalytic Performance and Phase Stability of Co3O4 in the Preferential Oxidation of Carbon Monoxide Studied In Situ, ACS Catal. 10 (2020) 11892–11911. doi:10.1021/acscatal.0c02653.

[26] L. Ma, C.Y. Seo, X. Chen, K. Sun, J.W. Schwank, Indium-doped Co3O4nanorods for catalytic oxidation of CO and C3H6towards diesel exhaust, Appl. Catal. B Environ. 222 (2018) 44–58. doi:10.1016/j.apcatb.2017.10.001.

[27] Q. Zhang, X. Liu, W. Fan, Y. Wang, Manganese-promoted cobalt oxide as efficient and stable non-noble metal catalyst for preferential oxidation of CO in H2stream, Appl. Catal. B Environ. 102 (2011) 207–214. doi:10.1016/j.apcatb.2010.11.043.

[28] Z. Zhao, T. Bao, Y. Zeng, G. Wang, T. Muhammad, Efficient cobalt-manganese oxide catalyst deposited on modified AC with unprecedented catalytic performance in CO preferential oxidation, Catal. Commun. 32 (2013) 47–51. doi:10.1016/j.catcom.2012.12.001.

[29] L.E. Gómez, E.E. Miró, A. V. Boix, Spectroscopic characterization of Mn-Co-Ce mixed oxides, active catalysts for COPROX reaction, Int. J. Hydrogen Energy. 38 (2013) 5645–5654. doi:10.1016/j.ijhydene.2013.03.004.

[30] M.T. Le, T.T. Nguyen, P.T.M. Pham, E. Bruneel, I. Van Driessche, Activated MnO2-Co3O4-CeO2 catalysts for the treatment of CO at room temperature, Appl. Catal. A Gen. 480 (2014) 34–41. doi:10.1016/j.apcata.2014.04.034.

[31] J.E. Park, E.D. Park, Effects of surface area of Co-Mn-O catalysts on the selective CO oxidation in H2, Catal. Letters. 144 (2014) 607–614. doi:10.1007/s10562-013-1185-1.

[32] Q. Guo, Y. Liu, MnOx modified Co3O4-CeO2 catalysts for the preferential oxidation of CO in H2-rich gases, Appl. Catal. B Environ. 82 (2008) 19–26. doi:10.1016/j.apcatb.2008.01.007.

[33] Z. Zhao, T. Bao, Y. Li, X. Min, D. Zhao, T. Muhammad, The supported CeO2/Co3O4-MnO2/CeO2catalyst on activated carbon prepared by a successive-loading approach with superior catalytic activity and selectivity for CO preferential oxidation in H2-rich stream, Catal. Commun. 48 (2014) 24–28. doi:10.1016/j.catcom.2014.01.017.

[34] W.Y. Hernández, M.A. Centeno, F. Romero-Sarria, S. Ivanova, M. Montes, J.A. Odriozola, Modified cryptomelane-type manganese dioxide nanomaterials for preferential oxidation of CO in the presence of hydrogen, in: Catal. Today, Elsevier, 2010: pp. 160–165. doi:10.1016/j.cattod.2010.03.010.

[35] Q. Guo, S. Chen, Y. Liu, Y. Wang, Stability of Co-Ce-Mn mixed-oxide catalysts for CO preferential oxidation in H2-rich gases, Chem. Eng. J. 165 (2010) 846–850. doi:10.1016/j.cej.2010.10.029.

[36] Z. Zhao, X. Lin, R. Jin, G. Wang, T. Muhammad, MO x (M=Mn, Fe, Ni or Cr) improved supported Co 3O 4 catalysts on ceria-zirconia nanoparticulate for CO preferential oxidation in H 2-rich gases, Appl. Catal. B Environ. 115–116 (2012) 53–62. doi:10.1016/j.apcatb.2011.12.001.

[37] Z. Zhao, R. Jin, T. Bao, H. Yang, X. Lin, G. Wang, Mesoporous Ce x Mn 1-x O 2 composites as novel alternative carriers of supported Co 3 O 4 catalysts for CO preferential oxidation in H 2 stream, Int. J. Hydrogen Energy. 37 (2012) 4774–4786. doi:10.1016/j.ijhydene.2011.12.057.

[38] L.E. Gómez, A. V. Boix, E.E. Miró, Co/ZrO2, Co/CeO2and MnCoCe structured catalysts for COPrOx, Catal. Today. 216 (2013) 246–253. doi:10.1016/j.cattod.2013.05.010.

[39] Z. Zhao, R. Jin, Y. Li, Y. Dai, T. Muhammad, Mesostructured Co-Ce-Zr-Mn-O composite as a potential catalyst for efficient removal of carbon monoxide from hydrogen-rich stream, Catal. Sci. Technol. 3 (2013) 2130–2139. doi:10.1039/c3cy00154g.

[40] Q. Zhang, X. Liu, W. Fan, Y. Wang, Manganese-promoted cobalt oxide as efficient and stable non-noble metal catalyst for preferential oxidation of CO in H2 stream, Appl. Catal. B Environ. 102 (2011) 207–214. doi:10.1016/j.apcatb.2010.11.043.

[41] Z. Zhao, Y. Li, T. Bao, G. Wang, T. Muhammad, Hierarchically nanoporous Co-Mn-O/FeOxas a high performance catalyst for CO preferential oxidation in H2-rich stream, Catal. Commun. 46 (2014) 28–31. doi:10.1016/j.catcom.2013.11.019.

[42] L. Zhong, T. Kropp, W. Baaziz, O. Ersen, D. Teschner, R. Schlögl, M. Mavrikakis, S. Zafeiratos, Correlation between Reactivity and Oxidation State of Cobalt Oxide Catalysts for CO Preferential Oxidation, ACS Catal. 9 (2019) 8325–8336. doi:10.1021/acscatal.9b02582.

[43] K. Frey, V. Iablokov, G. Sáfrán, J. Osán, I. Sajó, R. Szukiewicz, S. Chenakin, N. Kruse, Nanostructured MnOx as highly active catalyst for CO oxidation, J. Catal. 287 (2012) 30–36. doi:10.1016/j.jcat.2011.11.014.

[44] K. Ramesh, L. Chen, F. Chen, Y. Liu, Z. Wang, Y.F. Han, Re-investigating the CO oxidation mechanism over unsupported MnO, Mn2O3 and MnO2 catalysts, Catal. Today. 131 (2008) 477–482. doi:10.1016/j.cattod.2007.10.061.

[45] L.C. Wang, Q. Liu, X.S. Huang, Y.M. Liu, Y. Cao, K.N. Fan, Gold nanoparticles supported on manganese oxides for low-temperature CO oxidation, Appl. Catal. B Environ. 88 (2009) 204–212. doi:10.1016/j.apcatb.2008.09.031.

[46] L. Michel, S. Sall, T. Dintzer, C. Robert, A. Demange, V. Caps, Graphene-supported 2D cobalt oxides for catalytic applications, Faraday Discuss. (2019). doi:10.1039/C9FD00110G.

[47] G. Couvret, G. Genay, C. Robert, L. Michel, V. Caps, Intercalation of Copper Phthalocyanine Within Bulk Graphite as a New Strategy Toward the Synthesis of CuO-Based CO Oxidation Catalysts, Front. Chem. 8 (2020) 735. doi:10.3389/fchem.2020.00735.

[48] A. Bishnoi, S. Kumar, N. Joshi, Chapter 9 - Wide-Angle X-ray Diffraction (WXRD): Technique for Characterization of Nanomaterials and Polymer Nanocomposites, in: S. Thomas, R. Thomas, A.K. Zachariah, R.K.B.T.-M.M. in N.C. Mishra (Eds.), Micro Nano Technol., Elsevier, 2017: pp. 313–337. doi:https://doi.org/10.1016/B978-0-323-46141-2.00009-2.

[49] R. Follath, M. Hävecker, G. Reichardt, K. Lips, J. Bahrdt, F. Schäfers, P. Schmid, The energy materials in-situ laboratory Berlin (EMIL) at BESSY II, in: J. Phys. Conf. Ser., 2013: p. 212003. doi:10.1088/1742-6596/425/21/212003.

[50] S. Hendel, F. Schäfers, M. Hävecker, G. Reichardt, M. Scheer, J. Bahrdt, K. Lips, The EMIL project at BESSY II: Beamline design and performance, in: AIP Conf. Proc. 1741, 2016: p. 030038. doi:10.1063/1.4952861.

[51] C. Castán-Guerrero, D. Krizmancic, V. Bonanni, R. Edla, A. Deluisa, F. Salvador, G. Rossi, G. Panaccione, P. Torelli, A reaction cell for ambient pressure soft x-ray absorption spectroscopy, Rev. Sci. Instrum. 89 (2018) 054101. doi:10.1063/1.5019333.

[52] D.H. Simonne, A. Martini, M. Signorile, A. Piovano, L. Braglia, P. Torelli, E. Borfecchia, G. Ricchiardi, THORONDOR : a software for fast treatment and analysis of low-energy XAS data, J. Synchrotron Radiat. 27 (2020) 1741–1752. doi:10.1107/s1600577520011388.

[53] B. Gilbert, B.H. Frazer, A. Belz, P.G. Conrad, K.H. Nealson, D. Haskel, J.C. Lang, G. Srajer, G. De Stasio, Multiple scattering calculations of bonding and X-ray absorption spectroscopy of manganese oxides, J. Phys. Chem. A. 107 (2003) 2839–2847. doi:10.1021/jp021493s.

[54] B. Ravel, M. Newville, ATHENA, ARTEMIS, HEPHAESTUS: data analysis for X-ray absorption spectroscopy using IFEFFIT, J. Synchrotron Rad. 12 (2005) 537–541.

[55] L. Zhong, S. Zafeiratos, The chicken or the egg dilemma: is it the oxidation state of catalyst that determines the reactivity or the opposite?, n.d. doi:in prearation.

[56] E.S. Ilton, J.E. Post, P.J. Heaney, F.T. Ling, S.N. Kerisit, XPS determination of Mn oxidation states in Mn (hydr)oxides, Appl. Surf. Sci. 366 (2016) 475–485. doi:10.1016/j.apsusc.2015.12.159.

[57] D.E. Parry, Atomic calculation of photoionization cross-sections and asymmetry parameters J.-J. YEH, Rapid Commun. Mass Spectrom. 8 (1994) 579.

[58] W. Smekal, W.S.M. Werner, C.J. Powell, Simulation of electron spectra for surface analysis (SESSA): A novel software tool for quantitative Auger-electron spectroscopy and X-ray photoelectron spectroscopy, Surf. Interface Anal. 37 (2005) 1059–1067. doi:10.1002/sia.2097.

[59] Q. Cheng, Y. Tian, S. Lyu, N. Zhao, K. Ma, T. Ding, Z. Jiang, L. Wang, J. Zhang, L. Zheng, F. Gao, L. Dong, N. Tsubaki, X. Li, Confined small-sized cobalt catalysts stimulate carbon-chain growth reversely by modifying ASF law of Fischer–Tropsch synthesis, Nat. Commun. 9 (2018). doi:10.1038/s41467-018-05755-8.

[60] O.A. Bulavchenko, E.Y. Gerasimov, T.N. Afonasenko, Reduction of double manganese-cobalt oxides:: In situ XRD and TPR study, Dalt. Trans. 47 (2018) 17153–17159. doi:10.1039/c8dt04137g.

[61] T.E. Feltes, L. Espinosa-Alonso, E. de Smit, L. D'Souza, R.J. Meyer, B.M. Weckhuysen, J.R. Regalbuto, Selective adsorption of manganese onto cobalt for optimized Mn/Co/TiO2 Fischer-Tropsch catalysts, J. Catal. 270 (2010) 95–102. doi:10.1016/j.jcat.2009.12.012.

[62] R. Yang, Z. Xia, Z. Zhao, F. Sun, X. Du, H. Yu, S. Gu, L. Zhong, J. Zhao, Y. Ding, Z. Jiang, Characterization of CoMn catalyst by in situ X-ray absorption spectroscopy and wavelet analysis for Fischer–Tropsch to olefins reaction, J. Energy Chem. 32 (2019) 118–123. doi:10.1016/j.jechem.2018.07.005.

[63] W. Han, F. Dong, W. Han, Z. Tang, Fabrication of homogeneous and highly dispersed CoMn catalysts for outstanding low temperature catalytic oxidation performance, New J. Chem. 43 (2019) 12846–12857. doi:10.1039/c9nj03450a.

[64] Y. V. Golikov, S.Y. Tubin, V.P. Barkhatov, V.F. Balakirev, Phase diagrams of the CoMnO system in air, J. Phys. Chem. Solids. 46 (1985) 539–544. doi:10.1016/0022-3697(85)90215-X.

[65] E. Rios, J.L. Gautier, G. Poillerat, P. Chartier, Mixed valency spinel oxides of transition metals and electrocatalysis: Case of the MnxCo3-xO4 system, Electrochim. Acta. 44 (1998) 1491–1497. doi:10.1016/S0013-4686(98)00272-2.

[66] F. Morales, D. Grandjean, A. Mens, F.M.F. De Groot, B.M. Weckhuysen, X-ray absorption spectroscopy of Mn/Co/TiO2 fischer-tropsch catalysts: Relationships between preparation method, molecular structure, and catalyst performance, J. Phys. Chem. B. 110 (2006) 8626–8639. doi:10.1021/jp0565958.

[67] J.M.J. Mateos, J. Morales, J.L. Tirado, Cation-deficient Mn, Co spinel oxides obtained by thermal decomposition of carbonate precursors, J. Solid State Chem. 82 (1989) 87–94. doi:10.1016/0022-4596(89)90226-0.

[68] J. Gao, Y. Wang, Y. Ping, D. Hu, G. Xu, F. Gu, F. Su, A thermodynamic analysis of methanation reactions of carbon oxides for the production of synthetic natural gas, RSC Adv. 2 (2012) 2358–2368. doi:10.1039/c2ra00632d.

[69] V. Papaefthimiou, T. Dintzer, V. Dupuis, A. Tamion, F. Tournus, A. Hilion, D. Teschner, M. Hävecker, A. Knop-Gericke, R. Schlögl, S. Zafeiratos, A. Hillion, D. Teschner, M. Hävecker, A. Knop-Gericke, R. Schlögl, S. Zafeiratos, Nontrivial redox behavior of nanosized cobalt: New insights from ambient pressure X-ray photoelectron and absorption spectroscopies, ACS Nano. 5 (2011) 2182–2190. doi:10.1021/nn103392x.

[70] M.C. Biesinger, B.P. Payne, A.P. Grosvenor, L.W.M. Lau, A.R. Gerson, R.S.C. Smart, Resolving surface chemical states in XPS analysis of first row transition metals, oxides and hydroxides: Cr, Mn, Fe, Co and Ni, Appl. Surf. Sci. 257 (2011) 2717–2730. doi:10.1016/j.apsusc.2010.10.051.

[71] V. Di Castro, G. Polzonetti, XPS study of MnO oxidation, J. Electron Spectros. Relat. Phenomena. 48 (1989) 117–123. doi:10.1016/0368-2048(89)80009-X.

[72] H.W. Nesbitt, D. Banerjee, Interpretation of XPS Mn(2p) spectra of Mn oxyhydroxides and constraints on the mechanism of MnO2 precipitation, Am. Mineral. 83 (1998) 305–315. doi:10.2138/am-1998-3-414.

[73] I. Nakamura, M. Haneda, H. Hamada, T. Fujitani, Direct decomposition of nitrogen monoxide over a K-deposited Co(0 0 0 1) surface: Comparison to K-doped cobalt oxide catalysts, J. Electron Spectros. Relat. Phenomena. 150 (2006) 150–154. doi:10.1016/j.elspec.2005.01.295.

[74] S. Turczyniak, W. Luo, V. Papaefthimiou, N.S. Ramgir, M. Haevecker, A. MacHocki, S. Zafeiratos, A Comparative Ambient Pressure X-ray Photoelectron and Absorption Spectroscopy Study of Various Cobalt-Based Catalysts in Reactive Atmospheres, Top. Catal. 59 (2016) 532–542. doi:10.1007/s11244-015-0531-5.

[75] O.A. Bulavchenko, T.N. Afonasenko, S.S. Sigaeva, A. V. Ivanchikova, A.A. Saraev, E.Y. Gerasimov, V. V. Kaichev, S. V. Tsybulya, The Structure of Mixed Mn–Co Oxide Catalysts for CO Oxidation, Top. Catal. 63 (2020) 75–85. doi:10.1007/s11244-020-01230-1.

[76] S. Tanuma, C.J. Powell, D.R. Penn, Calculations of electron inelastic mean free paths (IMFPS). IV. Evaluation of calculated IMFPs and of the predictive IMFP formula TPP-2 for electron energies between 50 and 2000 eV, Surf. Interface Anal. 20 (1993) 77–89. doi:10.1002/sia.740200112.